



**MONTCLAIR STATE
UNIVERSITY**

Montclair State University

Montclair State University Digital
Commons

Theses, Dissertations and Culminating Projects

5-2023

Dynamics of Inertial and Non-Inertial Particles in Geophysical Flows

Nishanta Baral

Follow this and additional works at: <https://digitalcommons.montclair.edu/etd>



Part of the [Applied Mathematics Commons](#), and the [Applied Statistics Commons](#)

Abstract

We consider the dynamics of inertial and non-inertial particles in various flows. We investigate the underlying structures of the flow field by examining their Lagrangian coherent structures (LCS), which are found by computing finite-time Lyapunov exponents (FTLE). We compare the behavior of massless non-inertial particles using the velocity fields from four models, the Duffing oscillator, the Bickley jet, the double-gyre flow, and a quasi-geostrophic geophysical flow model, with that of inertial particles. For inertial particles with finite size and mass, we use the Maxey-Riley equation to describe the particle's motion. We explore the preferential aggregation of inertial particles and demonstrate how particle clustering depends on the density ratio, the Stokes number, and the particle size. We also study the effect of the Faxén correction and an often used assumption whereby the material derivative is set equal to the total derivative.

MONTCLAIR STATE UNIVERSITY

Dynamics of Inertial and Non-Inertial Particles in Geophysical Flows

by

Nishanta Baral

A Master's Thesis Submitted to the Faculty of

Montclair State University

In Partial Fulfillment of the Requirements

For the Degree of

Master of Science

May 2023

College of Science and Mathematics

Thesis Committee:

Department of Applied
Mathematics and Statistics

[REDACTED]
Dr. Eric Forgoston
Thesis Sponsor

[REDACTED]
Dr. David Trubatch
Committee Member

[REDACTED]
Dr. Ashwin Vaidya
Committee Member

Dynamics of Inertial and Non-Inertial Particles
in Geophysical Flows

A THESIS

Submitted in partial fulfillment of the requirements
For the degree of Master of Science

by

NISHANTA BARAL

Montclair State University

Montclair, NJ

May 2023

Acknowledgements

I would like to thank my advisor, Dr. Eric Forgoston, for his help and guidance with this thesis. This thesis would not have been possible without him.

I would also like to thank my committee members, Dr. David Trubatch and Dr. Ashwin Vaidya, for their input and support of my work.

I would also like to thank my family and friends for encouraging and motivating me in this process.

Contents

1	Introduction	6
2	Lagrangian Coherent Structures (LCS)	8
3	Maxey-Riley Equations	9
4	The Duffing Oscillator	12
4.1	Preferential Aggregation of Non-Inertial Particles	13
4.2	Preferential Aggregation of Inertial Particles	13
4.3	FTLE and iFTLE Fields	15
5	The Bickley Jet	16
5.1	Preferential Aggregation of Particles	17
5.2	Non-Inertial FTLE Field	18
5.3	Inertial iFTLE Field	19
6	Double-Gyre Fluid Flow	20
6.1	FTLE for Non-Inertial Particles	21
6.2	Dynamics of Inertial Particles	23
7	Quasi-Geostrophic Flow Model	26
7.1	FTLE Field for Non-Inertial Particles	28
8	Conclusions and Future Work	31

List of Figures

1	Four instances of coherent structures seen in nature. Starting from the top left and moving clock-wise: (a) temperature of the sea's surface in the Gulf Stream on April 18, 2005. The yellow colors signify warm waters, which appear to move in a snakelike pattern from the bottom left of the image to the top right of the image, forming a closed eddy at the northernmost end. The blue colors indicate colder waters dipping into the warmer waters of the Gulf Stream [16]; (b) coherent structures seen as the surface ocean current blows from the South Atlantic to the North Atlantic via the Gulf stream [17]; (c) a phytoplankton bloom off the coast of New Zealand's South Island as captured by NASA's Aqua satellite on November 13, 2017 [18]; and (d) lightly, moderately, and heavily oiled regions for the Gulf-facing beachfront of several barrier islands in eastern Mississippi on June 27, 2010, as captured by NASA's Earth Observing-1 satellite [19].	7
2	Preferential aggregation of non-inertial particles at time $t = 2.5$. A uniform grid of 64×64 non-inertial particles was seeded at time $t = 0$ throughout the domain of the Duffing oscillator with $\delta = 0.5$	14
3	Preferential aggregation of inertial particles at time $t = 2.5$. A uniform grid of 64×64 non-inertial particles were initialized at time $t = 0$ throughout the domain of the Duffing oscillator with $\delta = 0.5$. (Top) aerosols ($R = 0$) spread throughout much of the domain, while (bottom) bubbles ($R = 1$) coalesce near the center of the domain of the Duffing oscillator for Stokes numbers of (left) $St = 0.1$, (middle) $St = 0.2$, and (right) $St = 0.5$. The definitions of Stokes number and density ratio can be found in Eq. (14).	15
4	Forward-time FTLE and iFTLE fields in a Duffing Oscillator with $\delta = 0.1$ at $t = 2.5$ for (left) non-inertial particles, and for inertial particles with $St = 0.1$ and (middle) $R = 0$ and (right) $R = 1$	16
5	Preferential aggregation of non-inertial particles at (top) $t=7$, and (bottom) $t=10$ in a Bickley jet flow model.	17
6	Preferential aggregation of inertial particles in a Bickley jet flow model at time $t=10$ with $St = 0.1$ and (top) $R=0$, and (bottom) $R=1$. The definitions of Stokes number and density ratio can be found in	18
7	Forward-time FTLE field for non-inertial particles in a Bickley jet flow at (left) $t = 7$, and (right) $t = 10$	19
8	Forward-time iFTLE for inertial particles in a Bickley jet computed at $t = 10$ for (top) aerosols ($R = 0$), and (bottom) bubbles ($R = 1$) for Stokes numbers of (left) $St = 0.1$, (middle) $St = 0.2$, and (right) $St = 0.5$	20

9	Velocity field of the time-dependent double-gyre flow that demonstrates the periodic expansion and contraction of the gyres. The velocity fields are shown (top) at $t = 0$, with the separatrix located in the middle at $x = 1$, (middle) at $t = 2$, with the separatrix located in the left half of the domain, and (bottom) at $t = 7$, with the separatrix located in the right half of the domain	22
10	Forward-time FTLE field for (top panel) the time-independent case at (left) $t = 7.5$, (middle) $t = 15$, and (right) $t = 22.5$, and (bottom panel) the time-dependent case at (left) $t = 7.5$, (middle) $t = 15$, and (right) $t = 22.5$. The parameter values used in the computation are $A = 0.1$, $\omega = 6\pi/10$, and $\epsilon = 0.25$	23
11	Preferential aggregation for inertial particles at $t = 15$ for (top panel) aerosols, and for (bottom panel) bubbles, for a Stokes number of (left) $St = 0.1$, (middle) $St = 0.2$, and (right) $St = 0.5$. A uniform grid of 500×250 inertial particles were initialized at time $t = 0$ throughout the domain of the double-gyre flow. The parameter values used in the computation are $A = 0.1$, $\omega = 6\pi/10$, and $\epsilon = 0.25$	24
12	Preferential aggregation for inertial particles with $R = 1$ (bubbles) at $t = 15$ for the scenario where the total derivative is not assumed to be equal to the material derivative. The computations are performed for Stokes numbers of (left) $St = 0.1$, (middle) $St = 0.2$, and (right) $St = 0.5$. The parameter values used in the computation are	24
13	Forward-time FTLE field at time $t = 15$ for (top panel) aerosols, and for (bottom panel) bubbles, for a Stokes number of (left) $St = 0.1$, (middle) $St = 0.2$, and (right) $St = 0.5$. The parameter values used in the computation are $A = 0.1$, $\omega = 6\pi/10$, and $\epsilon = 0.25$	25
14	Forward-time iFTLE field computed with the MR equation including Faxén correction terms at time $t = 15$ for (top panel) aerosols, and for (bottom panel) bubbles, for a Stokes number of (left) $St = 0.1$, (middle) $St = 0.2$, and (right) $St = 0.5$, and $P = 1e-9$. The parameter values used in the computation are $A = 0.1$, $\omega = 6\pi/10$, and $\epsilon = 0.25$	26
15	Velocity field of the Stommel variant of the QG model with low periodic forcing ($\omega = 1$) at time $t = 3.73$. The velocity field shows two vertical gyres, namely the north gyre and the south gyre. There is a stronger flow magnitude on the left boundary of the domain as denoted by the color bar, which indicates the presence of the western boundary current in the QG model.	29
16	Forward-time FTLE fields for the QG model with frequency $\omega = 1$ after advecting the fluid particles through the flow map $\Phi_{0.1}^{2.1}$ (left), $\Phi_{1.25}^{3.25}$ (middle), and $\Phi_{2.5}^{4.5}$ (right) respectively. Low periodic sloshing preserves the gyre structure with high band of LCS encircling the gyres, and low FTLE values inside the gyres.	30

1 Introduction

The study of oceanic and atmospheric circulation is important for understanding a wide range of phenomena, such as weather and climate patterns, marine ecosystems, and the transport of contaminants. The atmospheric transport of particles (contaminants, dust, or other materials) is driven by atmospheric circulation patterns, and can range from spanning a localized area to spanning entire continents. A few examples include (a) an intense dust-storm, located over the Gobi desert on April 19, 1998, crossed the Pacific ocean in 5 days and settled down along the mountain ranges between the province of British Columbia in Canada and the state of California in the United States of America (USA) [1, 2], (b) during the 1970s and 1980s, lead isotopes which originated from Europe were transported southwards to Africa, and then westward via the trade winds to the island of Barbados in the Lesser Antilles [2], and (c) hurricane Ivan caused the transportation of soybean rust from South America to the Gulf coast of the USA [3].

Similarly, ocean circulation drives ocean transport with two significant examples being the Gulf stream transport and the Antarctic Circumpolar Current (ACC). Material transport across the Gulf stream is crucial for the North Atlantic climate as it drives mixing processes that influence sea surface temperature and chlorophyll [4]. Likewise, the ACC is the driving force for air-sea exchanges of heat, fresh water and atmospheric trace gases, and has a significant impact on global climate [5]. As such, the study of material transport in atmospheric and oceanic flows is of significant research interest. In particular, we would like to enhance our understanding of transport with one goal being accurate forecasting and prediction of various real-world situations, including how oil spills spread in the ocean, how different contaminants or rubbish is transported in the ocean [6], and how airborne microorganisms can be advected by atmospheric flows [3].

The accurate prediction of material transport requires an understanding of the underlying coherent structures within the flow. Coherent structures for geophysical fluid dynamics (GFD) flows provide a lower-dimensional description of the flow and enable the estimation of the fluid dynamics. Specifically, Lagrangian coherent structures (LCS) are important since they can be used to quantify material transport [7]. Because LCS provide a skeleton of the fluid flow, the study of coherent structures has proven to be important for many applications in a wide variety of fields, including atmospheric science [8], engineering [9], pollution reduction [9], population dynamics [10], oceanography [11], vehicle loitering [12], path planning [13, 14], and wave propagation [15]. Figure 1 shows four images which depict coherent structures that can be found in nature.

LCS are material lines that organize fluid-flow transport and may be viewed as the extensions of stable and unstable manifolds to general time-dependent systems [6, 20]. LCS describe the most repelling, attracting, and shearing material surfaces of a flow field which leads to a simpler understanding of flow geometry, an accurate understanding of material transport, and the potential to predict large-scale flow patterns and mixing events [21]. In two-dimensional (2D) flows, LCS are one-dimensional (1D) separating boundaries analogous to ridges defined by local maximum instability, and

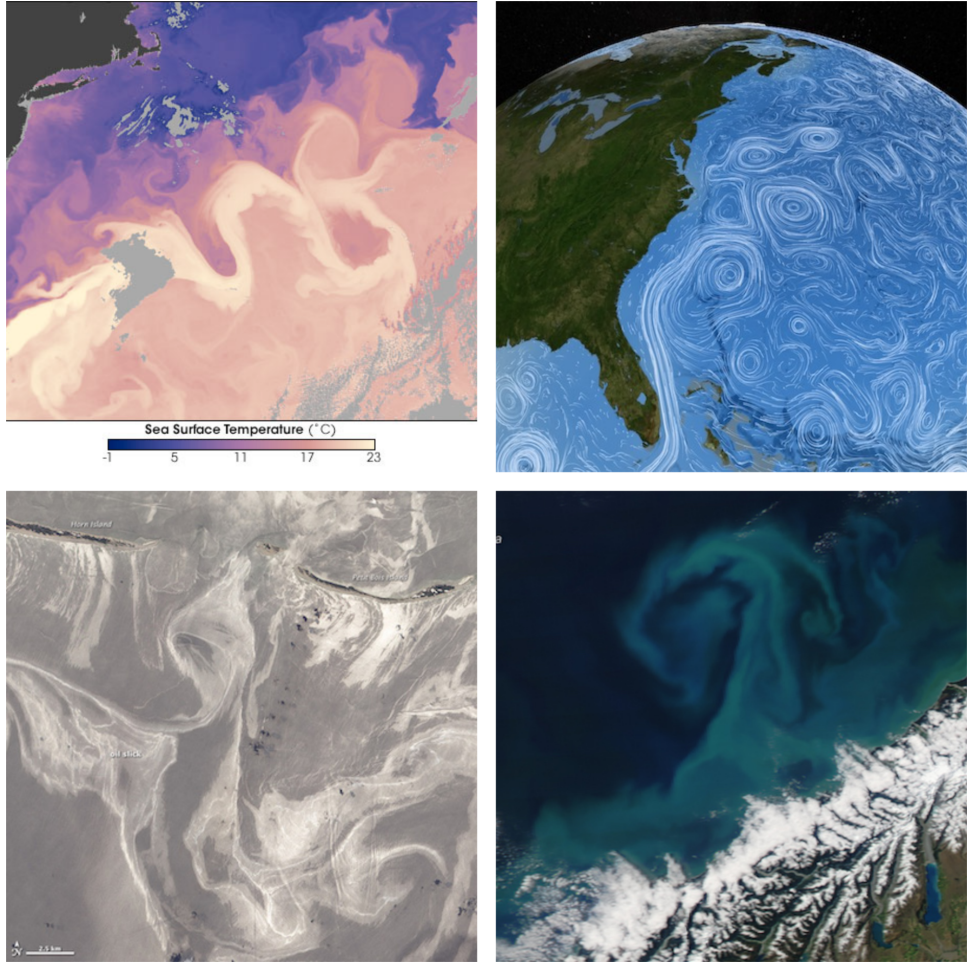


Figure 1: Four instances of coherent structures seen in nature. Starting from the top left and moving clock-wise: (a) temperature of the sea’s surface in the Gulf Stream on April 18, 2005. The yellow colors signify warm waters, which appear to move in a snakelike pattern from the bottom left of the image to the top right of the image, forming a closed eddy at the northernmost end. The blue colors indicate colder waters dipping into the warmer waters of the Gulf Stream [16]; (b) coherent structures seen as the surface ocean current blows from the South Atlantic to the North Atlantic via the Gulf stream [17]; (c) a phytoplankton bloom off the coast of New Zealand’s South Island as captured by NASA’s Aqua satellite on November 13, 2017 [18]; and (d) lightly, moderately, and heavily oiled regions for the Gulf-facing beachfront of several barrier islands in eastern Mississippi on June 27, 2010, as captured by NASA’s Earth Observing-1 satellite [19].

can be quantified by local measures of finite-time Lyapunov Exponents (FTLE) [7,21].

Numerous studies have been performed over the past few decades to find LCS and to understand the role they play in a variety of atmospheric and oceanic flows. There has also been a number of studies in which unmanned aerial vehicles (UAVs) [3], autonomous underwater vehicles (AUVs) and autonomous surface vehicles (ASVs) have been used to track LCS [6, 20], and to use knowledge of LCS for a wide array

of sensing tasks [7, 12, 22, 23]. The use of unmanned sensors and vehicles in this way enables improvements in our knowledge of ocean dynamics which then enables better understanding of ocean ecosystems and ocean health. In particular, the knowledge gleaned from the different sensing tasks will lead to improved understanding of how natural and man-made materials (algae, oil, rubbish, etc.) are transported on the surface and underwater, and will improve our understanding of weather and climate prediction.

Importantly, the tracking and sensing strategies mentioned above were derived using a highly abstracted kinematic model of the vehicle which neglects shape and inertial effects due to the finite size and mass of the vehicle or sensor. In fact, nearly all existing techniques for extracting and analyzing coherent structures are limited to theoretical point particles which are neutrally buoyant. Since LCS, computed via the FTLE, describe the transport of infinitesimal, massless objects in a flow, finite-size particles with mass do not follow these same trajectories. Instead, one must compute inertial FTLE (iFTLE) to find the inertial LCS which describe the transport of inertial particles. Therefore, in this thesis, we will investigate the interplay between inertial effects and transport in a variety of flows. We will use the Maxey-Riley (MR) equation to generate velocity fields for inertial particles, and show how the FTLE and iFTLE differ for each flow as a function of particle density ratio and Stokes number. We will also perform studies of how particles aggregate relative to the LCS for different parameter values. Lastly, we undertake a study of the effect of several assumptions often made when working with the MR equation.

2 Lagrangian Coherent Structures (LCS)

As mentioned in the Introduction, LCS are material lines that organize fluid-flow transport and may be viewed as the extensions of stable and unstable manifolds to general time-dependent systems [6, 20]. LCS can be studied by (a) identifying uniformly hyperbolic trajectories on a fixed portion of time and then growing their associated finite-time invariant manifolds, (b) constructing stable and unstable manifolds of fluid flows, or (c) deriving a measure of hyperbolic stretching and defining LCS as the most hyperbolic structures [24]. The third approach is the most commonly used approach to study LCS in the literature. A commonly used quantity to measure hyperbolic stretching is the finite-time Lyapunov exponent (FTLE) [8], which calculates the rate of separation between two nearby passive tracer particles over a finite time period [15]. The ridges of the FTLE represent the material lines in the flow field that are the most kinematically active [25]. Specifically, LCS explains the attracting, repelling, and shearing behavior of material lines over time and is a useful tool for describing complex flow dynamics [26].

To compute the finite-time Lyapunov exponent field, we consider an arbitrary two-dimensional velocity field defined on a domain D and a defined time interval $I = [t_0, t_0 + T]$. Fixing the initial time, t_0 , and a desired finite time, T , a flow map advects a particle starting at time t_0 from its initial position x_0 to its corresponding

position at the final time $t_0 + T$. The flow map, $\Phi_{t_0}^t$, is given as

$$\Phi_{t_0}^t : r_0 \mapsto r(r_0, t_0, t) = r_0 + \int_{t_0}^t u(r(\tau), \tau) d\tau, \quad (1)$$

where $u(r, t)$ is the fluid velocity field and $r(t)$ is the particle trajectory [12]. The FTLE is then given as

$$\sigma(x, t_0 + T, T) = \frac{1}{|T|} \ln \left(\sqrt{\lambda_{\max}(\Delta)} \right), \quad (2)$$

where

$$\Delta(x, t_0 + T, T) = \left(\frac{d\phi_{t_0}^{t_0+T}(x(t))}{dx(t)} \right)^* \left(\frac{d\phi_{t_0}^{t_0+T}(x(t))}{dx(t)} \right)$$

is the right Cauchy-Green deformation tensor, $*$ denotes the adjoint, and $\lambda_{\max}(\Delta)$ is the associated maximum eigenvalue of Δ [12].

We compute FTLE values at every point in the domain to obtain the FTLE field for the flow for a chosen finite time. Areas in which nearby particles separate exponentially over time will have high FTLE values, while regions where nearby particles stay close together will yield low FTLE values. Ridges of high FTLE values will correspond to LCS.

3 Maxey-Riley Equations

As discussed in the Introduction, the dynamics of inertial particles is different to that of passive tracer particles in a fluid flow as the motion of inertial particles can depict behavior such as clustering and dispersion [27]. The study of preferential aggregation of inertial particles in specific regions of a flow is of great significance due to its practical implications [28]. Our objective in this work is to explore the preferential aggregation of inertial particles and their corresponding iFTLE field in various flows for varying Stokes number and density ratios.

To obtain the FTLE field for inertial particles (iFTLE), we use the Maxey-Riley (MR) equation [29], given as

$$m_p \dot{v} = m_f \frac{D}{Dt} u(r(t), t) - \frac{1}{2} m_f \frac{d}{dt} [v - u(r(t), t) - \frac{1}{10} a^2 \nabla^2 u(r(t), t)] - 6\pi a \mu X(t) + (m_p - m_f) g - 6\pi a^2 \mu \int_0^t d\tau \frac{\frac{dX(\tau)}{d\tau}}{\sqrt{\pi v(t-\tau)}}, \quad (3)$$

with

$$X(t) = v(t) - u(r(t), t) - \frac{1}{6} a^2 \nabla^2 u.$$

Equation (3) is valid for two-dimensional (2D) or three-dimensional (3D) flows, where $r(t)$ denotes the position of a spherical particle at time t , $v(t) = \dot{r}(t)$ is the corresponding velocity of the particle, m_p is the mass of the inertial particle, m_f is the

mass of the fluid displaced by the particle, $u(r(t), t)$ is the velocity of the fluid at the location $r(t)$ and time t , μ is the viscosity of the underlying fluid, a is the radius of the particle, and g is the acceleration due to gravity. In Eq. (3), the derivative Du/Dt is the material derivative, and d/dt is the usual total derivative.

We non-dimensionalize the MR equation given by Eq. (3) using the velocity scale, U , and the length scale, L , of the external flow. As demonstrated by Cartwright et al. [30], we introduce the non-dimensional variables \hat{r} , \hat{u} , and \hat{t} in the following way: $r \rightarrow \hat{r}L$, $u \rightarrow \hat{u}U$, and $t = \frac{L}{U}\hat{t}$. Thus, $\dot{r} = U\hat{r}$ and $\ddot{r} = \frac{U^2}{L}\hat{\ddot{r}}$. The $a^2\nabla^2u$ term is the Faxén correction term. The Faxén correction term is non-dimensionalized as $\nabla^2u \rightarrow \frac{U}{L^2}\hat{\nabla}\hat{u}$. The integral term on the right-hand side of Eq. (3) is the Basset-Boussinesq history term. However, we choose to neglect it based on the assumption that the time interval for a particle to revisit a region it has visited earlier is large in comparison to the time scale of the problem [31]. Removing the Basset-Boussinesq term from Eq. (3) leads to a simplified form of the Maxey-Riley equation, given as

$$\begin{aligned} m_p\dot{v} &= m_f \frac{D}{Dt}u(r(t), t) - \frac{1}{2}m_f \frac{d}{dt}[v - u(r(t), t) - \frac{1}{10}a^2\nabla^2u(r(t), t)] \\ &\quad - 6\pi a\mu[v(t) - u(r(t), t) - \frac{1}{6}a^2\nabla^2u] + (m_p - m_f)g. \end{aligned} \tag{4}$$

Writing Eq. (4) in terms of the non-dimensional scalings as stated previously, one obtains

$$\begin{aligned} \frac{U^2}{L}m_p\ddot{\hat{r}} &= m_f \frac{U^2}{L} \frac{D\hat{u}}{D\hat{t}} - \frac{1}{2}m_f \frac{U^2}{L} \frac{\ddot{\hat{r}}}{\hat{t}} + \frac{1}{2}m_f \frac{U^2}{L} \frac{d\hat{u}}{d\hat{t}} + \frac{1}{20}m_f a^2 \frac{U^2}{L^3} \frac{d(\hat{\nabla}^2\hat{u})}{d\hat{t}} \\ &\quad - 6\pi a\mu[U\dot{\hat{r}} - \hat{u}U - \frac{1}{6}a^2 \frac{U}{L^2} \hat{\nabla}^2\hat{u}] + (m_p - m_f)g. \end{aligned} \tag{5}$$

Collecting the $\ddot{\hat{r}}$ terms on the left-hand side of Eq. (5), one has

$$\begin{aligned} \frac{U^2}{L}m_p\ddot{\hat{r}} + \frac{1}{2}m_f \frac{U^2}{L} \frac{\ddot{\hat{r}}}{\hat{t}} &= m_f \frac{U^2}{L} \frac{D\hat{u}}{D\hat{t}} + \frac{1}{2}m_f \frac{U^2}{L} \frac{d\hat{u}}{d\hat{t}} + \frac{1}{20}m_f a^2 \frac{U^2}{L^3} \frac{d(\hat{\nabla}^2\hat{u})}{d\hat{t}} \\ &\quad - 6\pi a\mu[U\dot{\hat{r}} - \hat{u}U - \frac{1}{6}a^2 \frac{U}{L^2} \hat{\nabla}^2\hat{u}] + (m_p - m_f)g, \end{aligned} \tag{6}$$

which can be rewritten as

$$\begin{aligned} \left(\frac{U^2}{L}(m_p + \frac{1}{2}m_f)\right)\ddot{\hat{r}} &= m_f \frac{U^2}{L} \frac{D\hat{u}}{D\hat{t}} + \frac{1}{2}m_f \frac{U^2}{L} \frac{d\hat{u}}{d\hat{t}} + \frac{1}{20}m_f a^2 \frac{U^2}{L^3} \frac{d(\hat{\nabla}^2\hat{u})}{d\hat{t}} \\ &\quad - 6\pi a\mu[U\dot{\hat{r}} - \hat{u}U - \frac{1}{6}a^2 \frac{U}{L^2} \hat{\nabla}^2\hat{u}] + (m_p - m_f)g. \end{aligned} \tag{7}$$

The material derivative, given by

$$\frac{Du}{Dt} = \frac{\partial u}{\partial t} + (u \cdot \nabla)u = \frac{\partial u}{\partial t} + u_x \frac{\partial u}{\partial x} + u_y \frac{\partial u}{\partial y}, \quad (8)$$

is the hydrodynamical derivative taken along the path of a fluid element, whereas the total derivative

$$\frac{du}{dt} = \frac{\partial u}{\partial t} + (v \cdot \nabla)u = \frac{\partial u}{\partial t} + \frac{\partial u}{\partial x} \frac{\partial x}{\partial t} + \frac{\partial u}{\partial y} \frac{\partial y}{\partial t}, \quad (9)$$

is taken along the particle's trajectory [30].

We reorder the terms in Eq. (7) in the form of *particle acceleration term* = *acceleration of the fluid element term* + *Stokes drag term* + *buoyancy effect term* + *terms involving the Faxén correction* so that

$$\begin{aligned} \left(\frac{U^2}{L}(m_p + \frac{1}{2}m_f)\right)\ddot{\hat{r}} &= m_f \frac{U^2}{L} \frac{D\hat{u}}{D\hat{t}} + \frac{1}{2}m_f \frac{U^2}{L} \frac{d\hat{u}}{d\hat{t}} - 6\pi a \mu U [\dot{\hat{r}} - \hat{u}] + (m_p - m_f) g \\ &\quad + \frac{1}{20}m_f a^2 \frac{U^2}{L^3} \frac{d(\hat{\nabla}^2 \hat{u})}{d\hat{t}} + \pi a \mu a^2 \frac{U}{L^2} \hat{\nabla}^2 \hat{u}, \end{aligned} \quad (10)$$

which can be rewritten as

$$\begin{aligned} \ddot{\hat{r}} &= \frac{m_f \frac{U^2}{L}}{\left(\frac{U^2}{L}(m_p + \frac{1}{2}m_f)\right)} \frac{D\hat{u}}{D\hat{t}} + \frac{m_f \frac{U^2}{L}}{\left(\frac{U^2}{L}(m_p + \frac{1}{2}m_f)\right)} \frac{1}{2} \frac{d\hat{u}}{d\hat{t}} + \frac{6\pi a \mu U}{\left(\frac{U^2}{L}(m_p + \frac{1}{2}m_f)\right)} [\hat{u} - \dot{\hat{r}}] \\ &\quad + \frac{(m_p - m_f)}{\left(\frac{U^2}{L}(m_p + \frac{1}{2}m_f)\right)} g + \frac{\frac{1}{20}m_f a^2 \frac{U^2}{L^3} \frac{d(\hat{\nabla}^2 \hat{u})}{d\hat{t}}}{\left(\frac{U^2}{L}(m_p + \frac{1}{2}m_f)\right)} + \frac{\pi a \mu a^2 \frac{U}{L^2} \hat{\nabla}^2 \hat{u}}{\left(\frac{U^2}{L}(m_p + \frac{1}{2}m_f)\right)}. \end{aligned} \quad (11)$$

Further algebraic simplification of Eq. (11) leads to

$$\begin{aligned} \ddot{\hat{r}} &= \frac{m_f}{(m_p + \frac{1}{2}m_f)} \frac{D\hat{u}}{D\hat{t}} + \frac{m_f}{(m_p + \frac{1}{2}m_f)} \frac{1}{2} \frac{d\hat{u}}{d\hat{t}} + \frac{6\pi a \mu L}{U(m_p + \frac{1}{2}m_f)} [\hat{u} - \dot{\hat{r}}] \\ &\quad + \frac{(m_p - m_f)}{\left(\frac{U^2}{L}(m_p + \frac{1}{2}m_f)\right)} g + \frac{1}{20} \frac{a^2}{L^2} \frac{m_f}{m_p + \frac{1}{2}m_f} \frac{d(\hat{\nabla}^2 \hat{u})}{d\hat{t}} + \frac{1}{6} \frac{a^2}{L^2} \frac{6\pi a \mu L}{U(m_p + \frac{1}{2}m_f)} \hat{\nabla}^2 \hat{u}. \end{aligned} \quad (12)$$

The non-dimensional MR equation, including buoyancy and the Faxén correction, is given as

$$\begin{aligned} \ddot{r}(t) &= R \frac{D}{Dt} u(r(t), t) + \frac{1}{2} R \frac{d}{dt} u(r(t), t) + \frac{1}{St} [u(r(t), t) - \dot{r}(t)] + W n \\ &\quad + \frac{1}{20} P^2 R \frac{d(\nabla^2 u)}{dt} + \frac{1}{6} \frac{P}{St} \nabla^2 u, \end{aligned} \quad (13)$$

where

$$St^{-1} = \frac{6\pi a \mu L}{(m_p + \frac{1}{2}m_f) U}, \quad R = \frac{m_f}{m_p + \frac{1}{2}m_f}, \quad W = \frac{m_p - m_f}{6\pi a \mu U St} g, \quad \text{and} \quad P = \frac{a}{L}. \quad (14)$$

In Eq. (14), St is the Stokes number, defined as the ratio of the characteristic time of a particle to a characteristic time of the flow, R is the density ratio parameter, P is the ratio of the radius of particle size to the characteristic length of the flow, and n is the unit vector pointing in the direction of gravity [28]. If $R = 2/3$, the particles have the same density as that of the carrier fluid, and we refer to those particles as neutrally buoyant. If $R > 2/3$, then the particles are lighter than the carrier fluid, and we refer to them as bubbles. Similarly, particles with $R < 2/3$ are denser than the carrier fluid, and we refer to them as aerosols [28].

For the sake of simplicity, we ignore buoyancy effects, and the non-dimensional MR equation with Faxén correction has a final form given by

$$\begin{aligned} \ddot{r}(t) = & R \frac{D}{Dt} u(r(t), t) + \frac{1}{2} R \frac{d}{dt} u(r(t), t) + \frac{1}{St} [u(r(t), t) - \dot{r}(t)] \\ & + \frac{1}{20} P^2 R \frac{d(\nabla^2 u)}{dt} + \frac{1}{6} \frac{P}{St} \nabla^2 u. \end{aligned} \quad (15)$$

If the Faxén correction term, used to justify nonuniform flow effects encountered by the inertial particle is ignored, Eq. (15) simplifies to

$$\ddot{r}(t) = R \frac{D}{Dt} u(r(t), t) + \frac{1}{2} R \frac{d}{dt} u(r(t), t) + \frac{1}{St} [u(r(t), t) - \dot{r}(t)]. \quad (16)$$

It is often assumed that for sufficiently small particles, the total derivative d/dt is equal to the material derivative D/Dt . In that case, Eq. (16) reduces further to

$$\ddot{r}(t) = \frac{3}{2} R \frac{D}{Dt} u(r(t), t) + \frac{1}{St} [u(r(t), t) - \dot{r}(t)], \quad (17)$$

which is the form of the MR equation used by Sudharsan et al. [28]. In our work, we will consider Eqs. (15)-(17) to understand how the iFTLE and particle aggregation is affected by the Faxén correction and the assumption that the material derivative equals the total derivative. In sections 4, 5, and 6 we will consider three different types of flow, and explore the preferential aggregation of inertial particles and their iFTLE fields.

4 The Duffing Oscillator

The Duffing oscillator, or Duffing equation, is a relatively simple second-order differential equation used to describe the motion of a damped oscillator which has a potential more complicated than that used for the simple harmonic oscillator. Unlike the following examples, it does not describe a geophysical flow, but because its

solutions can exhibit chaotic behavior, the Duffing oscillator is a good example with which to begin our analysis. The most general form of the Duffing oscillator, can be written as

$$\ddot{x} + \delta\dot{x} + (\beta x^3 \pm \omega_0^2 x) = \gamma \cos(\omega t + \phi), \quad (18)$$

where δ is the damping term, the term on the right-hand side is the forcing term, and the parameter β represents a ‘hard spring’ for $\beta > 0$ and a ‘soft spring’ for $\beta < 0$ [32].

For our work, setting $\beta = 1$, $\omega_0 = 1$, and $\phi = 0$, and using the negative sign for the \pm option, Eq. (18) can be written as

$$\ddot{x} + \delta\dot{x} + (x^3 - x) = \gamma \cos(\omega t). \quad (19)$$

The second-order ordinary differential equation (ODE) given by Eq. (19) can be written as the system of first-order ODEs

$$\begin{aligned} \dot{x} &= y, \\ \dot{y} &= x - x^3 - \delta y + \gamma \cos(\omega t). \end{aligned} \quad (20)$$

If we consider the unforced case, then the system of equations given by Eq. (20) reduces to

$$\begin{aligned} \dot{x} &= y, \\ \dot{y} &= x - x^3 - \delta y. \end{aligned} \quad (21)$$

In Eq. (21), \dot{x} represents the x -component and \dot{y} represents the y -component of the velocity field for the Duffing oscillator.

4.1 Preferential Aggregation of Non-Inertial Particles

To explore the preferential aggregation of non-inertial particles in a Duffing oscillator flow field, we construct a $[-2 \times 2] \times [-2 \times 2]$ grid and initialize passive tracer particles on the mesh grid with a step size of 0.0625. Using a 4th-order Runge-Kutta method with a time integration step size of 0.01, the particle trajectory is then calculated by advecting the particles according to the velocity field. Figure 2 shows the preferential aggregation of the non-inertial particles at $t = 2.5$. We can observe the chaotic behavior of the particles as they are attracted toward the strange attractor.

4.2 Preferential Aggregation of Inertial Particles

To understand how the finite size and mass affects the dynamics of inertial particles in a Duffing oscillator flow model, we solve the MR equation, and explore the preferential concentration of inertial particles for various Stokes numbers and density ratios. As in the non-inertial case, 4096 inertial particles are initialized uniformly on a $[-2 \times 2] \times [-2 \times 2]$ grid. Using a 4th-order Runge-Kutta method with a time integration step size of 0.01,¹ the inertial particle trajectories are computed by integrating the MR

¹Although higher accuracy Runge-Kutta (RK) methods, including the Runge-Kutta-Fehlberg method (RKF45) or 4th-order RK method (RK4) with adaptive step sizes and error control, can be

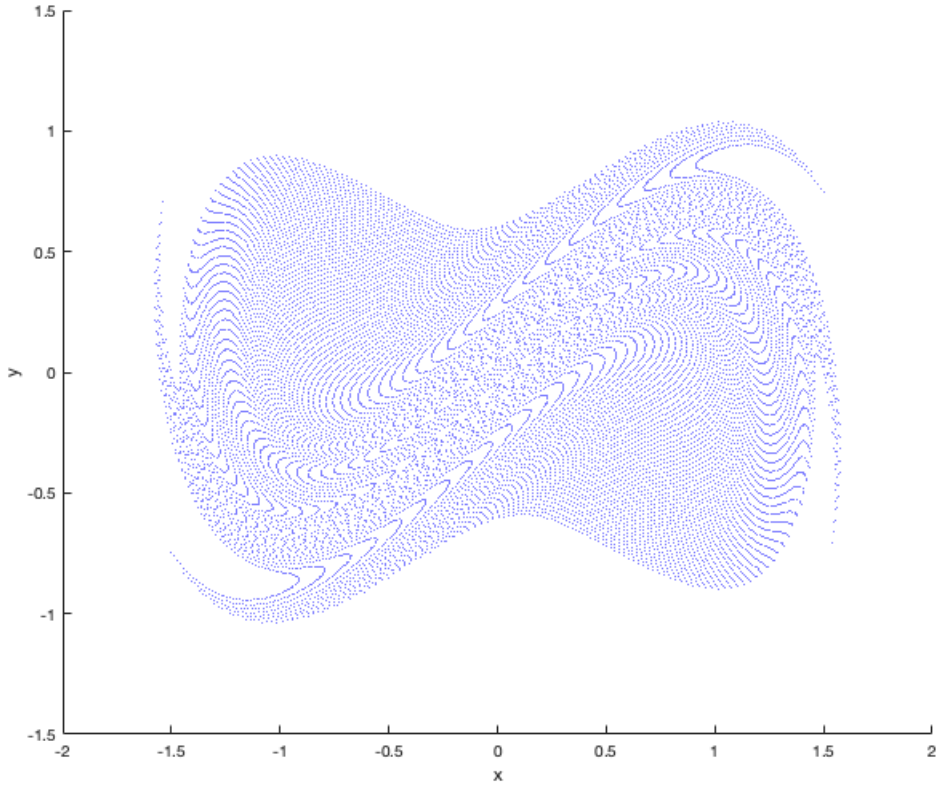


Figure 2: Preferential aggregation of non-inertial particles at time $t = 2.5$. A uniform grid of 64×64 non-inertial particles was seeded at time $t = 0$ throughout the domain of the Duffing oscillator with $\delta = 0.5$.

equation given by Eq. (17). Figure 3 shows the results for three different values of Stokes number ($St = 0.1, 0.2, 0.5$), and two different types of inertial particle, namely aerosols ($R = 0$) and bubbles ($R = 1$). One can see in the figure, paying attention to the scale of the axes, that aerosol particles spread throughout much of the domain, while bubbles coalesce in the center of the domain. It can also be noticed that with the increase in Stokes number, particles aggregate more rapidly towards their flow structures. Also, one can see that although aerosols are spread out across the domain, they have a denser core in the middle, while the opposite is true for bubbles. These density effects become more prominent as the Stokes number is increased.

used for more precise numerical solutions, we are forced to use a standard RK4 method with constant step-size due to the nature of the problem. Velocity field data is prescribed for a specified grid of constant step-size. Because the FTLE and iFTLE codes advect non-inertial and inertial particles respectively according to the grid used for the fluid velocity field, a constant step size must be used. Through the advection process, bi-linear interpolation is employed to obtain the fluid velocity data for non-grid points.

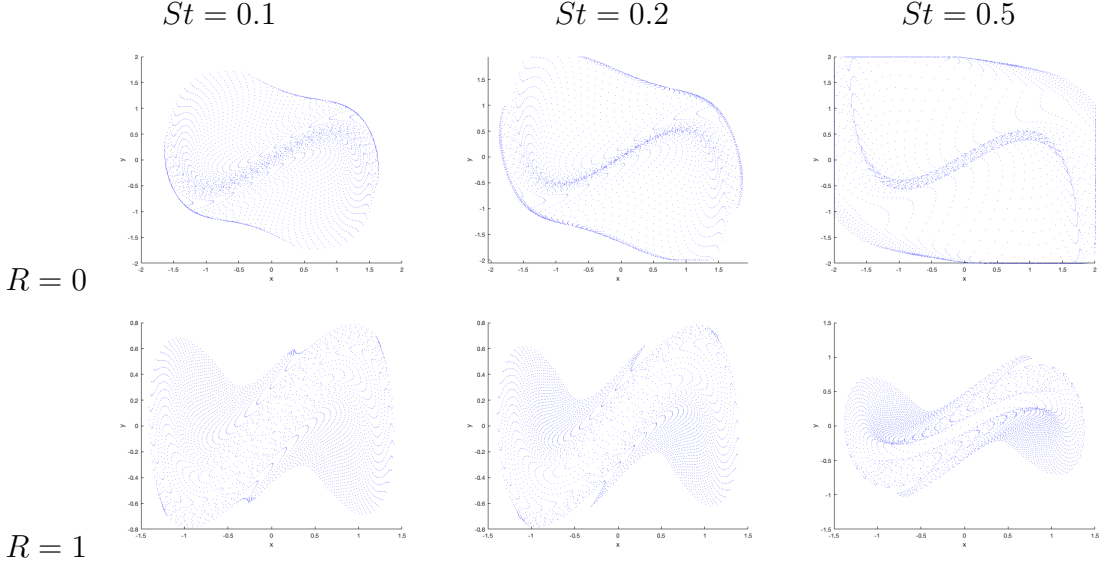


Figure 3: Preferential aggregation of inertial particles at time $t = 2.5$. A uniform grid of 64×64 non-inertial particles were initialized at time $t = 0$ throughout the domain of the Duffing oscillator with $\delta = 0.5$. (Top) aerosols ($R = 0$) spread throughout much of the domain, while (bottom) bubbles ($R = 1$) coalesce near the center of the domain of the Duffing oscillator for Stokes numbers of (left) $St = 0.1$, (middle) $St = 0.2$, and (right) $St = 0.5$. The definitions of Stokes number and density ratio can be found in Eq. (14).

4.3 FTLE and iFTLE Fields

We have also computed the FTLE and iFTLE fields to find the coherent structures of the Duffing oscillator for non-inertial and inertial particles. For both the FTLE and iFTLE computations, we construct a uniform mesh grid with step size of 0.03125 on the spatial domain of $[-2 \times 2] \times [-2 \times 2]$ and initialize the particles on the mesh grid. Using a 4th-order Runge-Kutta method with a time integration step size of 0.01, we calculate the non-inertial particle trajectories by advecting the particles according to the velocity field given by Eq. ((21)), while the inertial particle trajectories are computed for varying Stokes numbers and density ratios by integrating the MR equation given by Eq. (17). Then, the FTLE and iFTLE fields are calculated using Eq. (2) and the method described in section 2.

The non-inertial FTLE field, as shown in Fig. 4, highlights the strong arc-shaped coherent structure. For $St = 0.1$, the iFTLE field for bubbles ($R = 1$) is similar to the non-inertial case with a strong arc-shaped coherent structure. However, for aerosols ($R = 0$), the coherent structures become more spread out, showing the high separation of inertial particles throughout the center of the domain.

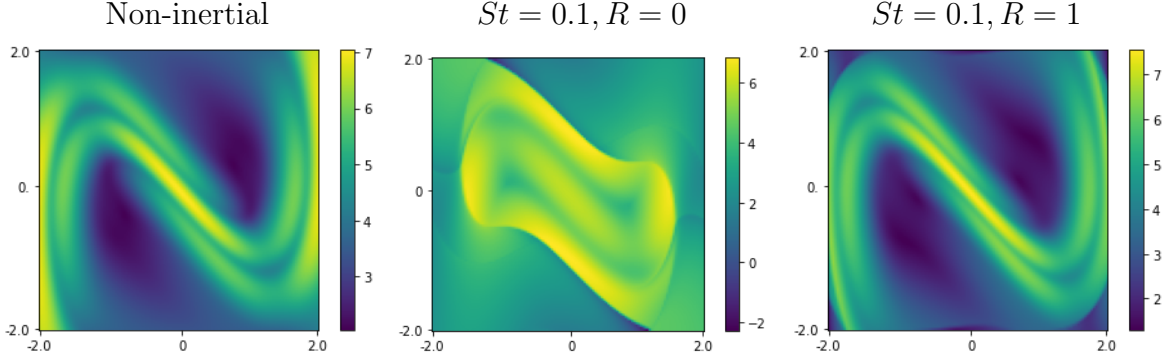


Figure 4: Forward-time FTLE and iFTLE fields in a Duffing Oscillator with $\delta = 0.1$ at $t = 2.5$ for (left) non-inertial particles, and for inertial particles with $St = 0.1$ and (middle) $R = 0$ and (right) $R = 1$.

5 The Bickley Jet

We now switch to the first of three types of geophysical fluid flows, a zonal flow. A zonal flow is a natural large-scale flow that follows latitudinal lines and occurs in both the ocean and the atmosphere [33]. Some examples of zonal flows are the Gulf stream, the polar night jet above Antarctica [33], and the East-West winds of Jupiter, Saturn, and Neptune [34]. We will consider the Bickley jet, which is an idealized model used to study the eastward zonal jet that is flanked by counter-rotating vortices. The Bickley jet is modeled by a time-dependent Hamiltonian, which is comprised of a steady background flow superimposed with a time-dependent perturbation [8,35].

The stream function is therefore modeled as

$$\psi(x, y, t) = \psi_0(y) + \psi_1(x, y, t), \quad (22)$$

with

$$\psi_0(y) = -UL \tanh\left(\frac{y}{L}\right), \quad (23)$$

and

$$\psi_1(x, y, t) = UL \operatorname{sech}^2\left(\frac{y}{L}\right) \operatorname{Re} \left[\sum_{n=1}^3 f_n(t) \exp(i k_n x) \right], \quad (24)$$

where $f_n(t) = \epsilon_n \exp(-ik_n c_n t)$. The steady background flow is given by $\psi_0(y)$, and $\psi_1(x, y, t)$ is the time-dependent perturbation. It is often convenient to expand $\psi_1(x, y, t)$ as

$$\psi_1(x, y, t) = UL \operatorname{sech}^2\left(\frac{y}{L}\right) (\epsilon_1 \cos(k_1(x - c_1 t)) + \epsilon_2 \cos(k_2(x - c_2 t)) + \epsilon_3 \cos(k_3(x - c_3 t))). \quad (25)$$

The velocity field for the Bickley jet model is computed as $\dot{x} = -\frac{\partial \psi}{\partial y}$ and $\dot{y} = \frac{\partial \psi}{\partial x}$. In Eqs. (22) - (24), U and L are the characteristic velocity scale and the characteristic length scale, respectively, and k_n , c_n , and ϵ_n represent the wave number, speed, and

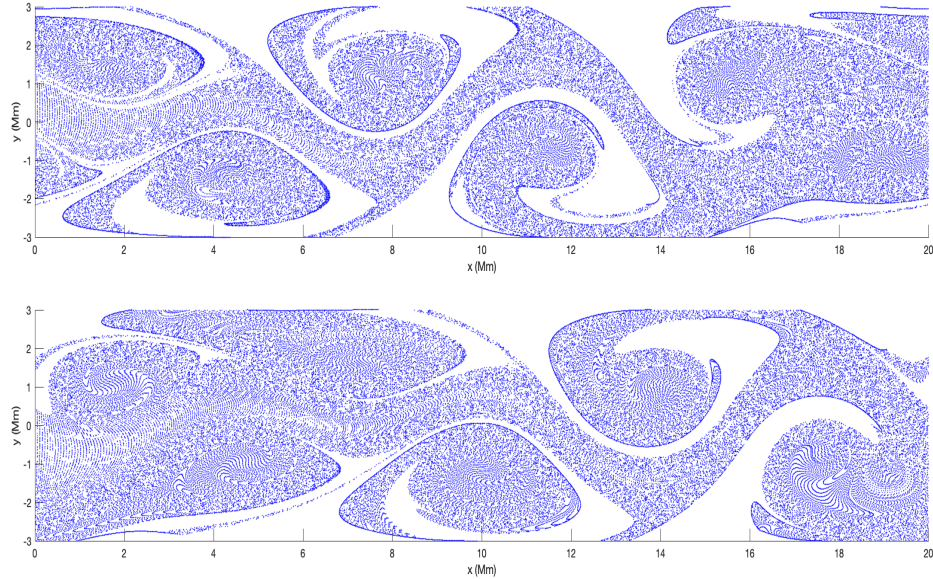


Figure 5: Preferential aggregation of non-inertial particles at (top) $t=7$, and (bottom) $t=10$ in a Bickley jet flow model.

amplitude, respectively, of the traveling Rossby waves. In our analysis, we use the parameter values of [8, 36, 37], which are set as $U = 5.413824 \text{ Mm}\cdot\text{day}^{-1}$, $L = 1.77 \text{ Mm}$, $k_n = 2/r_0$ where $r_0 = 6.371 \text{ Mm}$ is the mean radius of the earth, $\epsilon_1 = 0.075$, $\epsilon_2 = 0.4$, $\epsilon_3 = 0.3$, $c_3 = 0.461U$, $c_2 = 0.205U$, and $c_1 = c_3 + (\sqrt{5} - 1)(k_2/k_1)(c_2 - c_3)$. The parameters values are chosen to model how the stratospheric polar night jet stops the movement of ozone depleted air in the Southern hemisphere's late winter and early spring [37].

5.1 Preferential Aggregation of Particles

Just as was done for the Duffing oscillator, we explore the aggregation of non-inertial and inertial particles in a Bickley jet. For both scenarios, we consider 9000 particles initialized uniformly on a $[0 \times 20] \times [-3 \times 3]$ grid. Using a 4th-order Runge-Kutta method with a time integration step size of 0.01, the non-inertial particle trajectories are computed by advecting the particles according to the velocity field, while the inertial particle trajectories are computed by integrating the MR equation given by Eq. (17). Figure 5 shows the preferential aggregation of the non-inertial particles at $t = 7$ and $t = 10$. The aggregation of non-inertial particles follows the strong jet core and the counter-rotating vortices.

Figure 6 shows the preferential aggregation of aerosols ($R = 0$) and bubbles ($R = 1$) for $St = 0.1$ at $t = 10$. For aerosols, most particles aggregate in the strong jet core, and the vortices become enlarged, covering more of the spatial domain. In contrast, for bubbles, we do not see a strong aggregation of particles in the jet core. Rather, there is more of a blending of the vortices with the core, forming a spiral like

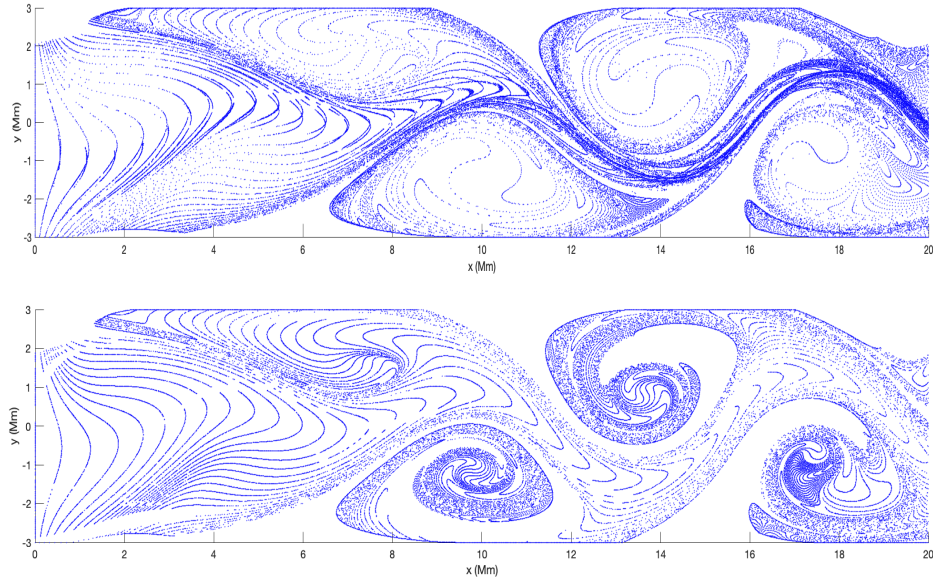


Figure 6: Preferential aggregation of inertial particles in a Bickley jet flow model at time $t=10$ with $St = 0.1$ and (top) $R=0$, and (bottom) $R=1$. The definitions of Stokes number and density ratio can be found in

Eq. (14).

structure. For both aerosols and bubbles, no appreciable difference can be found by varying the Stokes number.

5.2 Non-Inertial FTLE Field

As with the Duffing oscillator, we calculate the FTLE field to find the coherent structures associated with the Bickley jet flow field. We initialize 9000 passive tracer particles uniformly on a $[0 \times 20] \times [-3 \times 3]$ grid. The velocity fields $[\dot{x}, \dot{y}]$ are obtained by computing derivatives of the stream function using central finite differences. Using a 4th-order Runge-Kutta method with a time integration step size of 0.01, we calculate the non-inertial particle trajectories by advecting the particles according to the velocity field. Since the particles inside the strong eastward zonal jet are quickly advected out of the domain, we implement periodic boundary conditions in the x direction. Thus, particles which leave the domain on the right-hand side of the jet, re-enter the jet on the left-hand side. Then, the FTLE fields are calculated using Eq. (2) and the method described in section 2.

Figure 7 shows the forward-time FTLE field for the Bickley jet at $t=7$ and $t=10$. The coherent structures seen in the figure highlight the strong eastward zonal jet, as discussed previously. Fluid particles inside the jet are swept away by the jet, while particles outside the jet can become trapped inside the vortices. Thus, the LCS, highlighted by yellow ridges of maximal FTLE, demarcates the separation between the jet core and the vortices. The jet core, therefore, acts as a particle transport

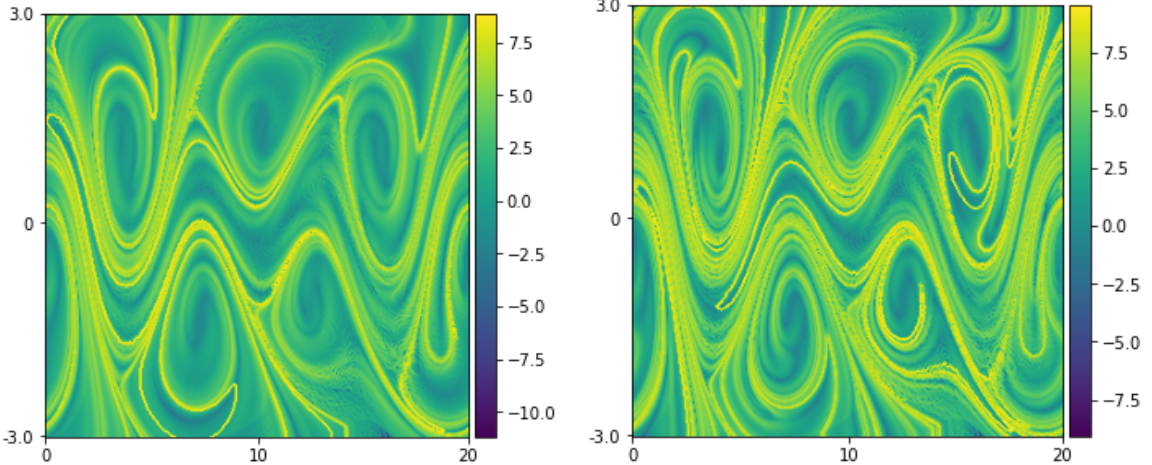


Figure 7: Forward-time FTLE field for non-inertial particles in a Bickley jet flow at (left) $t = 7$, and (right) $t = 10$.

barrier [8]. Fluid particles within the jet core stay together in the core, which leads to lower FTLE values within the core. As time increases, the FTLE ridges become stronger, as highlighted by the brighter yellow FTLE ridges on the right-most figure of Fig. 7.

5.3 Inertial iFTLE Field

To study the dynamics of inertial particles in a Bickley jet, we explore the iFTLE field computed for varying Stokes numbers and density ratios. We use the same combination of Stokes numbers and density ratios that was used in the Duffing oscillator flow model. As in the non-inertial case, 9000 inertial particles are initialized uniformly on a $[0 \times 20] \times [-3 \times 3]$ grid. Using a 4th-order Runge-Kutta method with a time integration step size of 0.01, the inertial particle trajectories are computed by integrating the MR equation given by Eq. (17).

Figure 8 shows the inertial iFTLE fields for the three Stokes numbers and for aerosols ($R = 0$) and bubbles ($R = 1$). In the case of aerosols, we see a band of maximal iFTLE ridges around the jet core as was seen in the FTLE field for non-inertial particles. However, the iFTLE ridges appear to be much denser in Fig. 8. As the Stokes number increases, both the maximal and minimal iFTLE values decrease slightly as seen from the color bar. There is not a significant difference in LCS structure for Stokes numbers lying between $St = 0.2$ and $St = 0.5$.

For bubbles, we see a band of maximal iFTLE ridges around the jet core, but the jet core is strongly preserved, and thus acts as a particle transport barrier as seen in Fig. 8. As the Stokes number increases, both the maximal and minimal iFTLE values increase slightly as seen from the color bar.

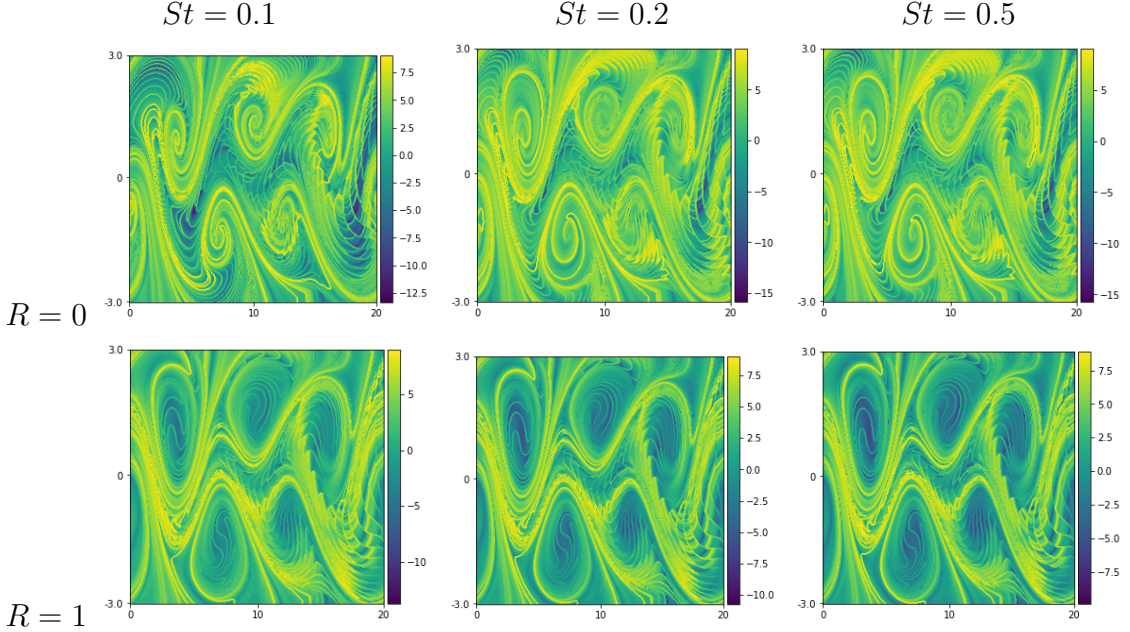


Figure 8: Forward-time iFTLE for inertial particles in a Bickley jet computed at $t = 10$ for (top) aerosols ($R = 0$), and (bottom) bubbles ($R = 1$) for Stokes numbers of (left) $St = 0.1$, (middle) $St = 0.2$, and (right) $St = 0.5$.

6 Double-Gyre Fluid Flow

We continue our analysis with the second geophysical flow, the double-gyre. The double-gyre flow is a simple and very well-studied fluid model consisting of two counter-rotating vortices, where the separatrix between vortices oscillates periodically to emulate wind forcing. The double-gyre flow is characterized by the stream function [12]

$$\psi(x, y, t) = A \sin(\pi f(x, t)) \sin(\pi y), \quad (26)$$

where

$$\begin{aligned} f(x, t) &= a(t)x^2 + b(t)x, \\ a(t) &= \epsilon \sin(\omega t), \\ b(t) &= 1 - 2\epsilon \sin(\omega t). \end{aligned} \quad (27)$$

Taking derivatives of the streamfunction, the velocity field for the double-gyre model is found to be

$$\begin{aligned} \dot{x} &= -\frac{\partial \psi}{\partial y} = -\pi A \sin(\pi f(x, t)) \cos(\pi y), \\ \dot{y} &= \frac{\partial \psi}{\partial x} = \pi A \cos(\pi f(x, t)) \sin(\pi y) \frac{df}{dx}, \end{aligned} \quad (28)$$

where $\frac{\omega}{2\pi}$ is the frequency of the separatrix oscillation, A is the approximate amplitude of the velocity vectors, and ϵ determines the amplitude of the left-right motion of the separatrix between the two gyres. When $\epsilon = 0$, the flow becomes time-independent,

and if $\epsilon \neq 0$, the gyres undergo a periodic expansion and contraction in the x direction [12]. In this work, we mostly focus on the time-dependent flow as it is more interesting and also more relevant to the more realistic quasi-geostrophic flow considered in the following section.

The double-gyre flow is usually studied on the rectangular spatial domain of $\Omega : [0 \times 2] \times [0 \times 1]$. For the time-independent case, one finds a steady flow with two counter-rotating gyres. One of the time-independent gyres is located on part of the domain at $\Omega_1 : [0 \times 1] \times [0 \times 1]$, while the second time-independent gyre is located on the part of the domain at $\Omega_2 : [1 \times 2] \times [0 \times 1]$. In the time-dependent case, the two gyres are separated by a heteroclinic manifold which connects the equilibrium points at $(1, 0)$ and $(1, 1)$. Thus, the separatrix acts as a barrier to particle transport. Figure 9 shows snapshots of the time-dependent velocity field at three different time instances which highlight the periodic left-right motion of the separatrix. In the time-independent case, the velocity field is steady and always has the form shown in Fig. 9 (a).

6.1 FTLE for Non-Inertial Particles

To calculate the FTLE field for non-inertial particles in a double-gyre flow, we initialize 500×250 passive tracer particles uniformly throughout the spatial domain. Using a 4th-order Runge-Kutta method with a time integration step size of 0.01, we calculate the non-inertial particle trajectories by advecting the particles according to the velocity field given in Eq. (28). Then, the FTLE fields are calculated using Eq. (2) and the method described in Sec. 2.

Figure 10 shows the FTLE field for the time-independent and time-dependent cases for finite times of $t = 7.5$, $t = 15$, and $t = 22.5$. For the time-independent case, one can see a ridge associated with maximal FTLE values which forms a transport barrier between the two gyres. This is the separatrix discussed previously. Infinitesimally close passive tracer particles located on opposite sides of the separatrix are advected exponentially far away from each other as time evolves. This FTLE ridge acts as a repelling coherent structure in forward time and as an attracting coherent structure in backward time. Looking at the FTLE fields at different times in the top row of Fig. 10, one sees that the FTLE field remains constant in time. This clearly makes sense since in the time-independent case, the flow is steady, and the velocity field is not changing in time.

However, for the time-dependent case, the flow is changing in time, and thus we see an FTLE field which evolves in time as seen in the bottom row of Fig. 10. One can also see the deformation of the ridge associated with the maximal FTLE values. Different from the time-independent case, the LCS denoted by the ridge of maximal FTLE values, is much more complicated, and cannot be seen by observing the velocity field. Note also that the density of high FTLE ridges increases with an increase in the finite time of integration.

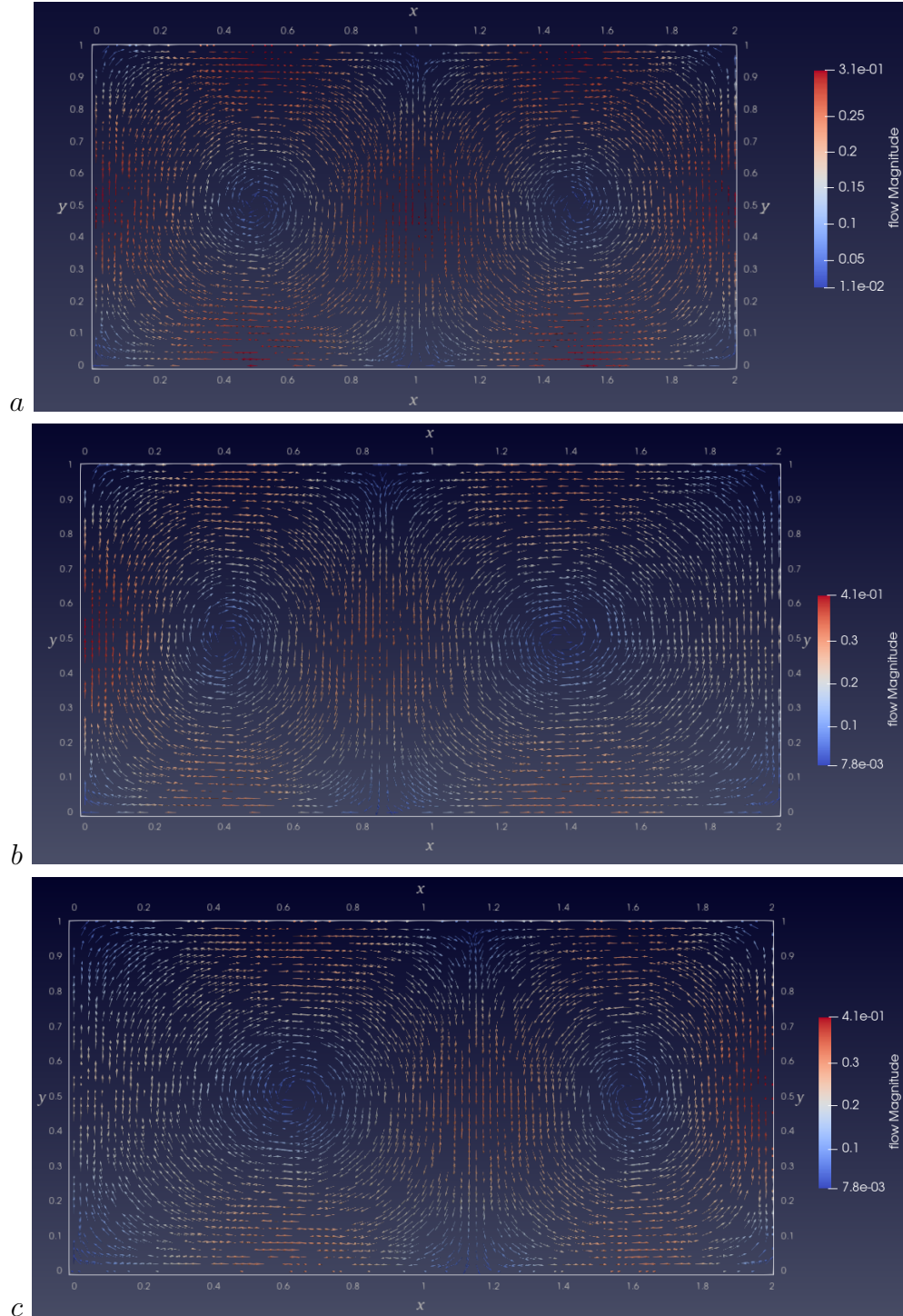


Figure 9: Velocity field of the time-dependent double-gyre flow that demonstrates the periodic expansion and contraction of the gyres. The velocity fields are shown (top) at $t = 0$, with the separatrix located in the middle at $x = 1$, (middle) at $t = 2$, with the separatrix located in the left half of the domain, and (bottom) at $t = 7$, with the separatrix located in the right half of the domain

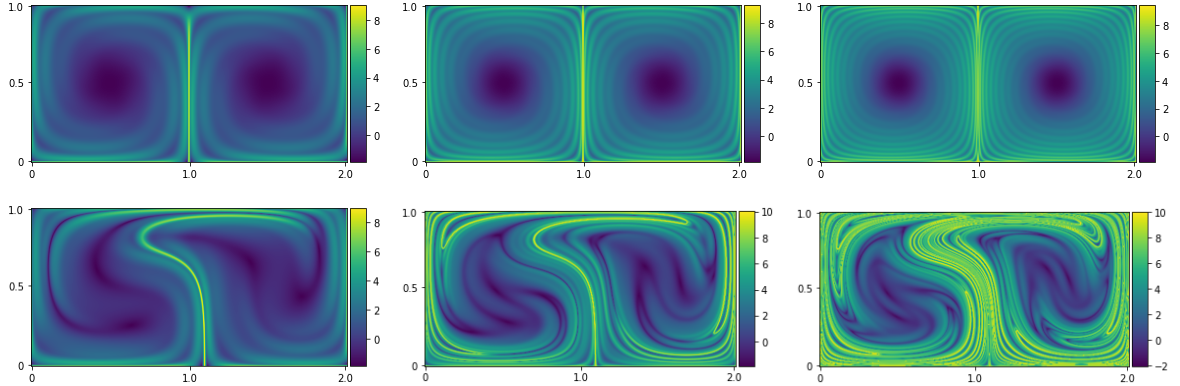


Figure 10: Forward-time FTLE field for (top panel) the time-independent case at (left) $t = 7.5$, (middle) $t = 15$, and (right) $t = 22.5$, and (bottom panel) the time-dependent case at (left) $t = 7.5$, (middle) $t = 15$, and (right) $t = 22.5$. The parameter values used in the computation are $A = 0.1$, $\omega = 6\pi/10$, and $\epsilon = 0.25$.

6.2 Dynamics of Inertial Particles

To understand the dynamics of inertial particles in a double-gyre flow model, we explore the preferential concentration of inertial particles and the inertial FTLE fields for various Stokes numbers and density ratios using Eq. (17). As described in Sec. 3, if $R = 2/3$, the particles are neutrally buoyant, and have the same density as that of the carrier fluid. If $R > 2/3$, then the particles are lighter than the carrier fluid, and we refer to them as bubbles. Lastly, particles with $R < 2/3$ are denser than the carrier fluid, and we refer to them as aerosols. Figure 11 shows the particle aggregation of aerosols and bubbles at time $t = 15$ after advecting the inertial particles using the MR equation given by Eq. (17) for varying Stokes number. We see that aerosols ($R = 0$) aggregate toward the maximal FTLE ridges while bubbles ($R = 1$) are repelled from the maximal FTLE ridges. Instead, bubbles form clusters in the center of the gyres. It can also be noticed that with the increase in Stokes number, particles aggregate more rapidly towards the FTLE ridge or gyre center, depending on whether they are bubbles or aerosols.

Qualitatively, there is excellent agreement between Fig. 11 and the results shown by Sudharsan et al. for these choices of St and R [28]. In Eq. (17), which is the form of the MR equation used by Sudharsan et al., it is assumed that for sufficiently small particle size, the total derivative and the material derivative are the same. However, in general, it is not necessarily the case that the material derivative and total derivative are identical. Therefore, we also examine the preferential aggregation for inertial particles using Eq. (16) which does not assume the two derivatives are equal.

For aerosols ($R = 0$) the particle trajectory doesn't depend on the fluid acceleration as the first term on the right hand side of Eq. (17) goes to 0. Thus, no effect of the difference between the total derivative and the material derivative is seen. Fig-

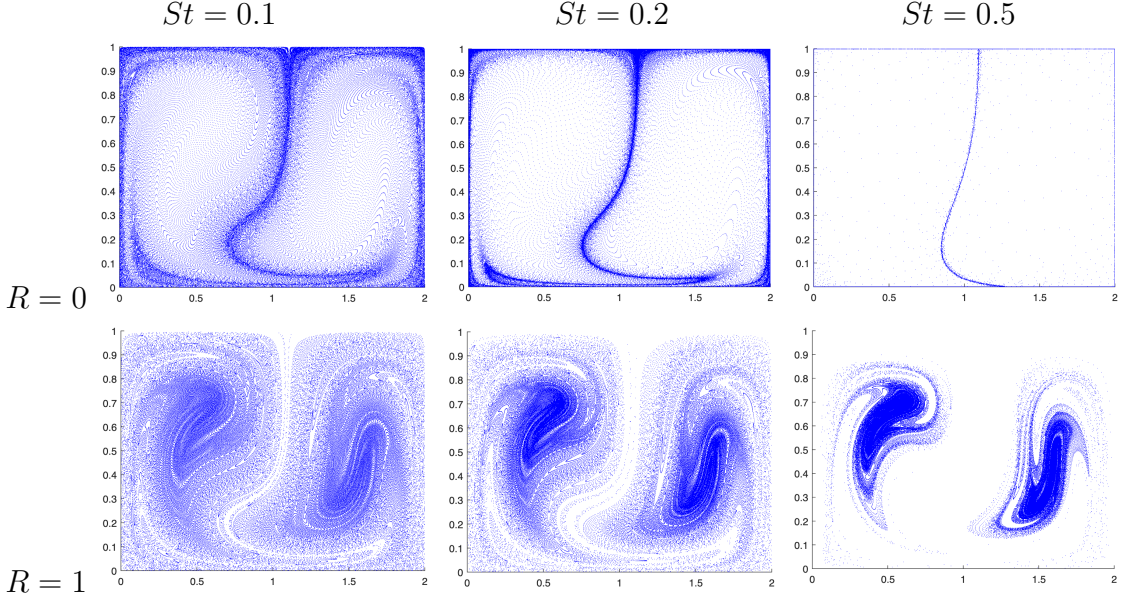


Figure 11: Preferential aggregation for inertial particles at $t = 15$ for (top panel) aerosols, and for (bottom panel) bubbles, for a Stokes number of (left) $St = 0.1$, (middle) $St = 0.2$, and (right) $St = 0.5$. A uniform grid of 500×250 inertial particles were initialized at time $t = 0$ throughout the domain of the double-gyre flow. The parameter values used in the computation are $A = 0.1$, $\omega = 6\pi/10$, and $\epsilon = 0.25$.

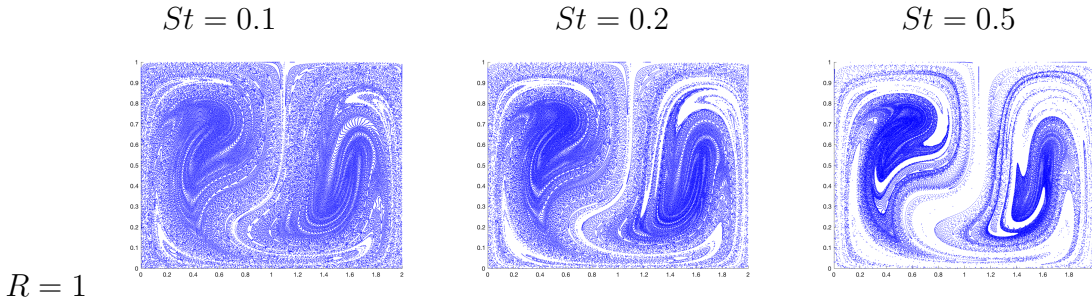


Figure 12: Preferential aggregation for inertial particles with $R = 1$ (bubbles) at $t = 15$ for the scenario where the total derivative is not assumed to be equal to the material derivative. The computations are performed for Stokes numbers of (left) $St = 0.1$, (middle) $St = 0.2$, and (right) $St = 0.5$. The parameter values used in the computation are

$$A = 0.1, \omega = 6\pi/10, \text{ and } \epsilon = 0.25.$$

Figure 12 shows the particle aggregation of bubbles ($R = 1$) at $t = 15$ when the total derivative and the material derivative are not assumed to be identical. Comparing the bottom panel of Fig. 11 with Fig. 12, we notice that even though the preferential aggregation is similar in that the particles are accruing in the gyre centers, the aggregation is occurring more slowly.

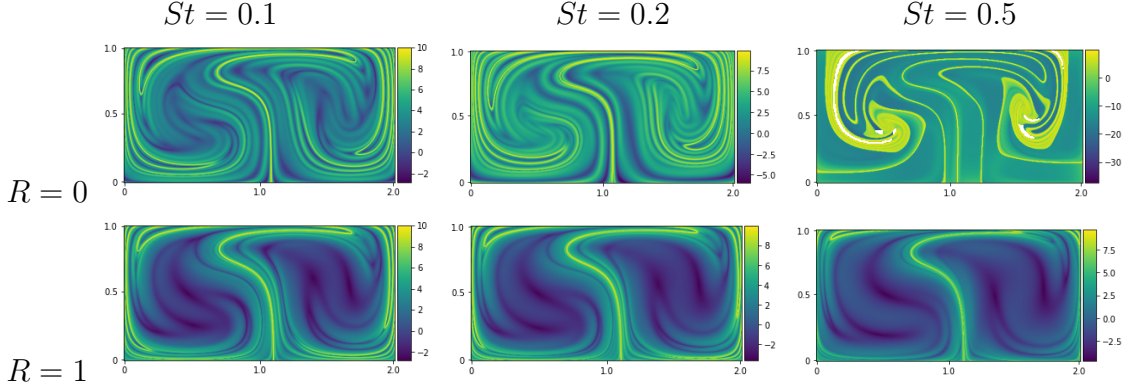


Figure 13: Forward-time FTLE field at time $t = 15$ for (top panel) aerosols, and for (bottom panel) bubbles, for a Stokes number of (left) $St = 0.1$, (middle) $St = 0.2$, and (right) $St = 0.5$. The parameter values used in the computation are $A = 0.1$, $\omega = 6\pi/10$, and $\epsilon = 0.25$.

We have also examined the inertial iFTLE fields for aerosols and bubbles in a double-gyre flow for varied Stokes numbers and density ratios. The forward-time iFTLE fields at $t = 15$ are shown in Fig. 13. For aerosols ($R = 0$), the iFTLE field looks similar to non-inertial particles up to $St = 0.2$. For $St = 0.5$, we see that there is a significant difference in the iFTLE field and the particles all end up clustering along an LCS which runs between the two gyres. For bubbles ($R = 1$), we see low FTLE values in the center of the gyres. This is consistent with particle aggregation inside each of the gyres as seen in Fig. 11.

As previously discussed in Sec. 3, the Faxén correction terms are typically ignored for small particle sizes. To study the effect of particle size in a double-gyre flow, we examine the iFTLE fields for aerosols and bubbles by including the Faxén correction terms in our computation. Initializing 500×250 inertial particles uniformly on our domain, and using a 4th-order Runge-Kutta method with a time integration step size of 0.1, the inertial particle trajectories are computed by integrating the MR equation given by Eq. (13) with nondimensional particle size parameter $P = 10^{-9}$. We use the same combinations of Stokes number and density ratio as used in the iFTLE computation when the Faxén corrections terms were not included, and the results are shown in Fig. 14. For aerosols ($R = 0$), the iFTLE field looks similar as without Faxén correction with only difference between the iFTLE field for $St = 0.5$. With the inclusion of the Faxén correction, particles aggregate more slowly towards the LCS, and thus no significant difference can be seen in the iFTLE field at time $t = 15$. For bubbles ($R = 1$), the iFTLE field looks similar as without the Faxén correction with the exception that stronger FTLE ridges are seen around the boundary of the gyres. There is no significant difference in the coherent structures with the increase in Stokes number. Note that the results do not appreciably change for a wide range of P values from $P = 10^{-15} - 10^{-6}$.

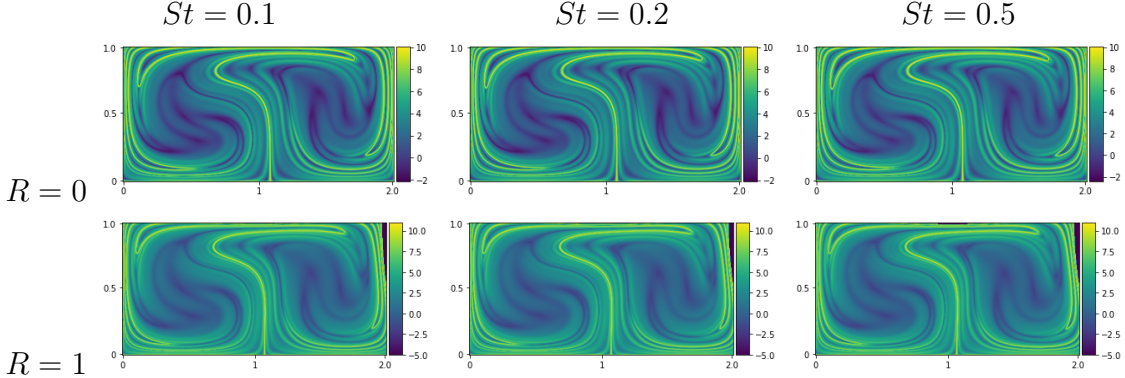


Figure 14: Forward-time iFTLE field computed with the MR equation including Faxén correction terms at time $t = 15$ for (top panel) aerosols, and for (bottom panel) bubbles, for a Stokes number of (left) $St = 0.1$, (middle) $St = 0.2$, and (right) $St = 0.5$, and $P = 1e-9$. The parameter values used in the computation are $A = 0.1$, $\omega = 6\pi/10$, and $\epsilon = 0.25$.

7 Quasi-Geostrophic Flow Model

The study of the overall circulation patterns of oceans and the collection of oceanographic data has been a topic of research for many years. One model, which is closely related to the double-gyre model, is a reduced ocean model known as the barotropic quasi-geostrophic (QG) model. Unlike the double-gyre model, the QG model is a partial differential equation (PDE) derived from first principles. The QG model has been used to describe the nature and variability of the Western boundary currents seen in the ocean [38], and continues to be a powerful model in studying emergent applications in ocean and climate research [11].

Although the derivation can be found in detail in Ref. [38], for completeness we provide a brief overview. The derivation begins by considering Sverdrup theory to obtain the relationship for geostrophic balance. We consider the momentum equation written in a rotating reference frame with the earth at an angular velocity Ω , given as

$$\frac{D\vec{u}}{Dt} + 2\vec{\Omega} \times \vec{u} = -\frac{\nabla p}{\rho} + \vec{g} + \frac{\mathfrak{I}}{\rho}, \quad (29)$$

where \vec{u} is the velocity seen in the rotating frame, p is the pressure, ρ is the density, \vec{g} is the acceleration due to gravity, and \mathfrak{I} is an implicit representation of turbulent momentum mixing effects of smaller scale motions.

A homogeneous layer of fluid of constant thickness, D , lies beneath a mixed layer in which the wind-driven turbulent stresses drive an Ekman transport. Under the layer, and in contact with the bottom, lies another viscous boundary layer in which viscous stresses produced by the motion couple the fluid to the solid bottom. If we assume that the flow is in geostrophic balance everywhere, the North-South scale of the motion is large enough to make the Rossby number small and, at the same time, small enough that the β plane approximation is valid. Then, the stream function can

be written as

$$\psi = \frac{p}{\rho f_0}, \quad (30)$$

where the fluid pressure is p , its density is ρ , and f_0 is the Coriolis parameter at the central latitude of the gyre. Similarly, the velocities can be found by differentiating the streamfunction so that

$$u = -\frac{\partial \psi}{\partial y}, \quad v = \frac{\partial \psi}{\partial x}. \quad (31)$$

The β plane approximation is the first-order approximation of the Coriolis force given as

$$f = f_0 + \beta y. \quad (32)$$

The relative vorticity is defined as

$$\zeta = \frac{\partial v}{\partial x} - \frac{\partial u}{\partial y}, \quad (33)$$

and it satisfies the momentum equation given as

$$\frac{d(\zeta + \beta y)}{dt} = (f_0 + \beta y + \zeta) \frac{\partial w}{\partial z} + A_H \nabla^2 \zeta. \quad (34)$$

The vorticity production caused by the stretching of the total vortex filaments by the vertical velocity is given by $(f_0 + \beta y + \zeta) \frac{\partial w}{\partial z}$, while $A_H \nabla^2 \zeta$ is the lateral diffusion of vorticity. Using a β plane approximation and geostrophic approximation, we obtain

$$f_0 + \beta y + \zeta \approx f_0. \quad (35)$$

Integrating Eq. (34) over the layer thickness, D , gives

$$\frac{d\zeta}{dt} + \beta v = \frac{f_0}{D} (w_E - w_B) + A_H \nabla^2 \zeta, \quad (36)$$

where w_B is the velocity pumped out of the lower boundary layer, and w_E is the Ekman velocity pumped out of (or into) the upper mixed layer. Ekman layer theory is used to represent w_B as

$$w_B = \frac{\delta_E}{2} \zeta, \quad (37)$$

where $\delta_E \ll D$. Now the vorticity equation can be written in terms of the stream function as

$$\frac{\partial}{\partial t} \nabla^2 \psi + J(\psi, \nabla^2 \psi) + \beta \frac{\partial \psi}{\partial x} = \frac{f_0}{D} w_E - r \nabla^2 \psi + A_H \nabla^4 \psi, \quad (38)$$

where $\zeta = \nabla^2 \psi$, and where J is the Jacobian operator given as

$$J(f, g) : \frac{\partial f}{\partial x} \frac{\partial g}{\partial y} - \frac{\partial g}{\partial x} \frac{\partial f}{\partial y}, \quad (39)$$

describing the advection of relative vorticity by the motion field.

We assume the upper Ekman pumping velocity to have the form used in Ref [39], so that

$$w_E = -\sin(2\pi y) + 2\alpha\pi \sin(\omega t). \quad (40)$$

We also assume that the flow is contained in a basin of characteristic length scale L and the Sverdrup balance is achieved for the interior. If U is a characteristic scale for the horizontal velocity, and W_E is a characteristic scale for the Ekman pumping, then in order to balance those two terms, we must have

$$U = W_E \frac{f_0}{\beta D}. \quad (41)$$

By non-dimensionalizing the stream function, ψ , and x and y , and scaling t by $1/\beta L$, one obtains

$$\frac{\partial}{\partial t} \nabla^2 \psi + \varepsilon J(\psi, \nabla^2 \psi) + \frac{\partial \psi}{\partial x} = w_E - \mu \nabla^2 \psi + E \nabla^4 \psi, \quad (42)$$

where the non-dimensional parameters are

$$\begin{aligned} \varepsilon &= \frac{U}{\beta L^2} = \left(\frac{\delta_I}{L}\right)^2, \\ \mu &= \frac{r}{\beta L} = \left(\frac{\delta_s}{L}\right), \\ E &= \frac{A_H}{\beta L^3} = \left(\frac{\delta_M}{L}\right)^3. \end{aligned} \quad (43)$$

The parameters ε , μ , and E measure the relative importance of nonlinearity, bottom friction, and lateral diffusion, respectively. We can see that the non-dimensional parameters are formulated with respect to the relative length scales of three important boundary layers: Stommel (δ_S), Munk (δ_M), and Inertial (δ_I). A combination of parameters is used to study different QG models, but we will study only the Stommel model in this work. The Stommel model is a steady state flow to resemble the North Atlantic basin by utilizing wind stress and the Coriolis force to create a boundary layer similar to the Gulf Stream [11]. The Stommel form of our model can be written as

$$\frac{\partial}{\partial t} \nabla^2 \psi + \varepsilon J(\psi, \nabla^2 \psi) + \frac{\partial \psi}{\partial x} = w_E - \mu \nabla^2 \psi, \quad (44)$$

where w_E provides the forcing of the model.

7.1 FTLE Field for Non-Inertial Particles

We study three different cases of the Stommel variant of the QG flow model with respect to its forcing frequency, namely $\omega = 1, 3, 9$. These frequencies represent low periodic forcing ($\omega = 1$), moderate periodic forcing ($\omega = 3$), and high periodic forcing ($\omega = 9$). The stream function of the QG model given by Eq. (44) involves a PDE, unlike the flows examined in Secs. 4, 5, and 6. PDEs are known for their complexity,

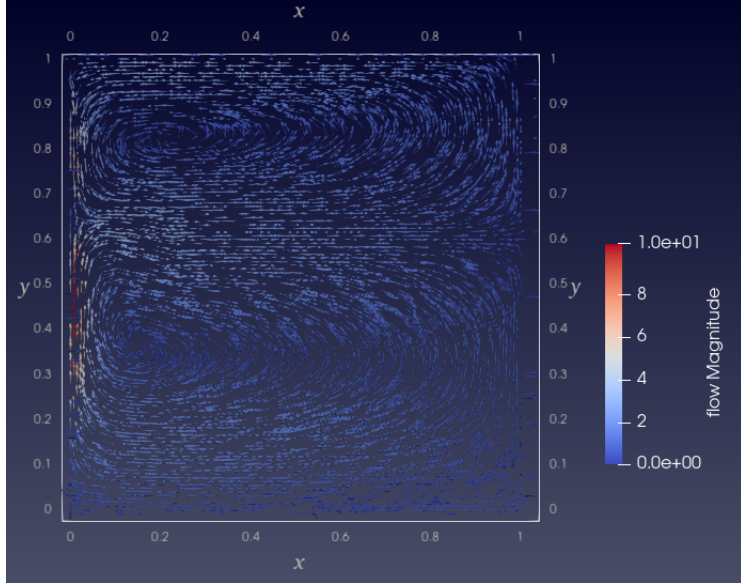


Figure 15: Velocity field of the Stommel variant of the QG model with low periodic forcing ($\omega = 1$) at time $t = 3.73$. The velocity field shows two vertical gyres, namely the north gyre and the south gyre. There is a stronger flow magnitude on the left boundary of the domain as denoted by the color bar, which indicates the presence of the western boundary current in the QG model.

and often do not have a closed-form analytical solution. The stream function of the QG model also does not have an analytical solution with which to find velocity field data. Therefore, the QG model was solved numerically to generate time-dependent velocity data with time stepping of 0.01. Figure 15 show a velocity field snapshot at time $t = 3.73$ of our QG model with $\omega = 1$.

As with the other flows studied in Secs. 4, 5, and 6, we calculate the FTLE field using the velocity field data generated by solving the QG model. We initialize 128×128 passive tracer particles uniformly on a $[0 \times 1] \times [0 \times 1]$ grid. Using a 4th-order Runge-Kutta method with a time integration step size of 0.01, we calculate the non-inertial particle trajectories by advecting the particles according to the velocity field data.

From our numerical computation, we have velocity field data at every grid point for our desired time interval. As the particles are advected for each time step, they will generally be positioned between the grid points. Therefore, we use a bi-linear interpolation scheme to calculate the velocity field data for particles which reside outside of grid points, which enables the continued advection of the particles for the next integration time step. Then, the FTLE fields are calculated using Eq. (2) and the method described in Sec. 2.

Figure 16 shows the FTLE field at low frequency ($\omega = 1$) computed at three different time intervals. We see LCS demarcating the structure of the gyres and almost no separation between the nearby particles inside the gyres. Similarly, Fig. 17

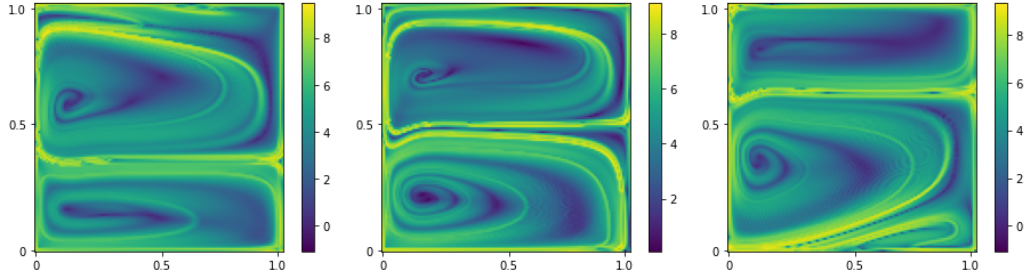


Figure 16: Forward-time FTLE fields for the QG model with frequency $\omega = 1$ after advecting the fluid particles through the flow map $\Phi_{0.1}^{2.1}$ (left), $\Phi_{1.25}^{3.25}$ (middle), and $\Phi_{2.5}^{4.5}$ (right) respectively. Low periodic sloshing preserves the gyre structure with high band of LCS encircling the gyres, and low FTLE values inside the gyres.

shows the FTLE field at moderate frequency ($\omega = 3$) computed at three different time instances. We see there are bands of LCS around the gyres, and more mixing between the gyres compared to the low frequency case. Finally, Fig. 18 shows the FTLE field at high frequency ($\omega = 9$) computed at different time periods. We observe thin FTLE ridges within the gyres, in addition to the band of LCS encircling the gyres. This is in contrast to the cases of low frequency and moderate frequency.

Unlike the other flows we have studied, we do not have the results for the dynamics of inertial particles in the QG flow. The dynamics of inertial particles in the QG flow is complex as the QG model is formulated in a rotating frame while the MR equation is not. However, because of the way the QG model is derived it is not straightforward to implement a Coriolis force in the MR equation. We are working on developing a method that enables us to match the Coriolis force from the QG model to a new Coriolis force term that we add to the MR equation. If one were to use the MR equation without a Coriolis force with QG velocity data, all of the inertial particles in the QG flow quickly aggregate on the boundaries, rather than aggregating along LCS or within gyres as expected.

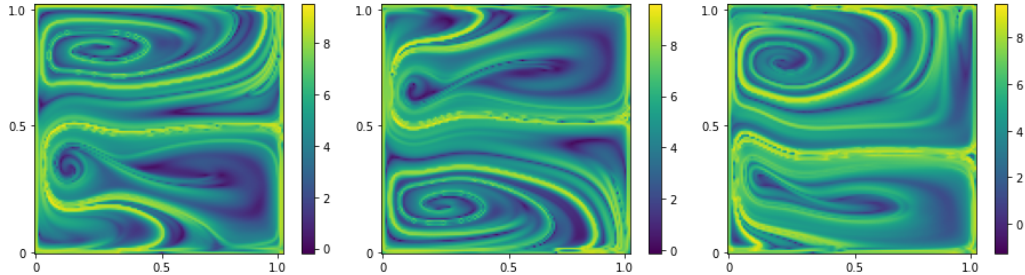


Figure 17: Forward-time FTLE fields for the QG model with frequency $\omega = 3$ after advecting the fluid particles through the flow map $\Phi_{0.1}^{2.1}$ (left), $\Phi_{1.25}^{3.25}$ (middle), and $\Phi_{2.5}^{4.5}$ (right) respectively. Moderate periodic sloshing slightly distorts the gyre structure, but bands of LCS remain around the gyres.

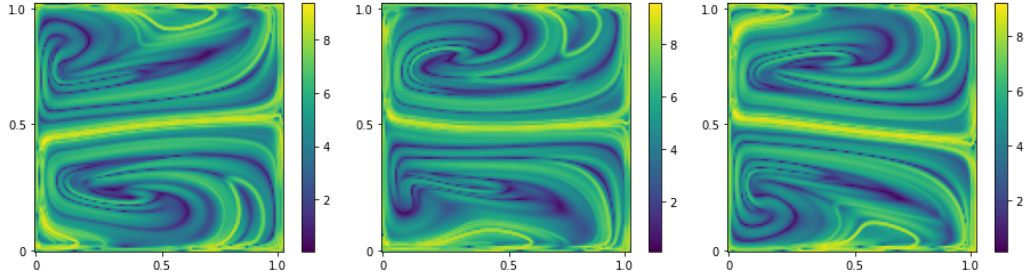


Figure 18: Forward-time FTLE fields for the QG model with frequency $\omega = 9$ after advecting the fluid particles through the flow map $\Phi_{0.1}^{2.1}$ (left), $\Phi_{1.25}^{3.25}$ (middle), and $\Phi_{2.5}^{4.5}$ (right) respectively. High periodic sloshing results in complicated LCS structure with ribboning of the LCS inside the gyres. We still observe the band of LCS around the gyres similar to the cases with low and moderate sloshing frequency.

8 Conclusions and Future Work

In this work, we wish to improve our understanding of material transport in various atmospheric and oceanic flows, which in turn enable us to make more accurate predictions for a variety of physical, biological and man-made phenomena. To do this, we explored the Lagrangian Coherent Structure (LCS) in various flows, namely the Duffing oscillator, Bickley jet, double-gyre flow, and quasi-geostrophic (QG) flow model, by computing their finite-time Lyapunov exponent (FTLE) field. Over the years in the literature, much work has been performed with infinitesimal passive tracer particles to understand the behavior of different flows. However, particles in the real-world have finite size and mass. These particles, also known as inertial particles, do not follow the same trajectory as passive tracer particles in a flow. Since little work has been performed to understand the relationship between inertial particles and the FTLE field, we implemented a comprehensive study. We used the Maxey-Riley equation in various forms to describe the particle’s motion and compare the particles’ behavior in various fluid flow models. We also explored the preferential aggregation of inertial particles and demonstrate how particle clustering depends on the density ratio and the Stokes number. The results were compared and contrasted with those of passive tracers.

We began our exploration with the Duffing oscillator whose solution can depict chaotic dynamics. Preferential aggregation of non-inertial particles in the Duffing oscillator displayed chaotic behavior of the particles as they aggregated onto the strange attractor. Similarly, we found that aerosols ($R = 0$) spread throughout much of the domain, while bubbles coalesced near the center of the domain. The FTLE field and iFTLE field for bubbles highlighted a strong arc-shaped coherent structure, while the iFTLE field for aerosols became more spread out in the domain.

Similarly, for the Bickley jet, non-inertial particles were swept along the strong jet core or moved throughout the counter-rotating vortices. In contrast, for inertial

particles, aerosols aggregated in the strong jet core and the vortices become enlarged covering more of the spatial domain. For bubbles, there was more of a blending of the vortices with the core, forming a spiral like structure. Non-inertial FTLE fields in the Bickley jet highlighted the strong eastwards zonal jet and the jet core where the jet core acted as a particle transport barrier. The iFTLE field for aerosols was found to be similar to the FTLE field, but iFTLE ridges appear to be much denser. Similarly, for bubbles we found the maximal iFTLE ridges around the jet core, but the jet core was strongly preserved which acted as a particle transport barrier.

We then explored the dynamics of non-inertial and inertial particles in the well studied double-gyre flow, which has a periodic left-right expansion and contraction of the gyres for the time-dependent case. We explored the FTLE field for the time-independent case, and showed how the maximal FTLE ridge denoting the LCS, which remains stationary in time, acts as the particle transport barrier. However, the FTLE field in the time-dependent case shows a deformation of the LCS. We also explored the aggregation of aerosols and bubbles in the double-gyre flow model. We found that aerosols aggregated toward the LCS while bubbles formed clusters in the center of the gyres.

One of the most common assumptions made when using the MR equation is that the total derivative and material derivative are identical. Since this is not true in general, we explored the preferential aggregation in bubbles when those two derivatives aren't assumed to be identical. We found that particle aggregation was identical although the fluid particles were slowly aggregating to their flow structure. Additionally, we explored the iFTLE field for varying Stokes number and density ratios where the forward time iFTLE ridges highlighted the repelling coherent structures. We also explored the iFTLE field including the Faxén correction terms in the MR equation. We found that the iFTLE field looks similar to the results without the Faxén correction, where the only difference is that the particles aggregated more slowly towards their flow structure. For bubbles, the iFTLE field looked similar as the case without the Faxén correction, with the exception that stronger LCS were seen around the boundary of the gyres.

Lastly, we explored the dynamics of non-inertial particles in a more realistic geophysical quasi-geostrophic flow. The QG flow model mimics the North Atlantic ocean with a strong western boundary current representing the Gulf Stream. We studied three different cases of the Stommel variant of the QG flow model with respect to its forcing frequency, namely $\omega = 1, 3, 9$. We found that a low periodic frequency ($\omega = 1$) preserved the gyre structure with a band of LCS encircling the gyres. A moderate periodic frequency ($\omega = 3$) slightly distorted the gyre structures and allowed more mixing between the gyres. A high periodic frequency ($\omega = 9$) highlighted even more mixing between the gyres and created more complicated looking coherent structures.

In the future, we plan to study the iFTLE field and aggregation dynamics for inertial particles in a QG flow by incorporating a rotating frame of reference with Coriolis force in the MR equation. Once completed, we will be able to perform a comprehensive study of inertial particle dynamics with varying Stokes number, density ratio, and particle size, as was performed here for the other types of flow. Also, as mentioned previously, the Basset-Boussinesq term in the original form of the

MR equation is often neglected. It is tricky to include this history term, but since it may play an important role in the dynamics, it is well-worth incorporating into our work. The we will be able to understand the role of this term in the dynamics of inertial particles for all of the flows we have studied as well as additional flows of interest.

Also of interest in the future is the exploration of machine learning (ML) methodologies. Fueled by large volumes of data, machine learning and data analytics have revolutionized a wide range of scientific disciplines in the last few years [11, 40–43]. We would like to extend the range of applications to the identification of coherent structures. Notably, reliable and efficient recognition of coherent structures can inform a fleet of autonomous vehicles to sample the ocean environment most effectively, and thus can significantly advance ocean prediction.

References

- [1] R. B. Husar, D. Tratt, B. A. Schichtel, S. Falke, F. Li, D. Jaffe, S. Gasso, T. Gill, N. S. Laulainen, F. Lu, et al., “Asian dust events of April 1998,” *Journal of Geophysical Research: Atmospheres*, vol. 106, no. D16, pp. 18317–18330, 2001.
- [2] A. Stohl, S. Eckhardt, C. Forster, P. James, and N. Spichtinger, “On the pathways and timescales of intercontinental air pollution transport,” *Journal of Geophysical Research: Atmospheres*, vol. 107, no. D23, pp. ACH–6, 2002.
- [3] A. E. Bozorg Magham, S. D. Ross, and D. G. Schmale III, “Real-time prediction of atmospheric Lagrangian coherent structures based on forecast data: An application and error analysis,” *Physica D: Nonlinear Phenomena*, vol. 258, pp. 47–60, 2013.
- [4] Y. Liu, C. Wilson, M. A. Green, and C. W. Hughes, “Gulf Stream transport and mixing processes via coherent structure dynamics,” *Journal of Geophysical Research: Oceans*, vol. 123, no. 4, pp. 3014–3037, 2018.
- [5] C. W. Böning, A. Dispert, M. Visbeck, S. Rintoul, and F. U. Schwarzkopf, “The response of the Antarctic Circumpolar Current to recent climate change,” *Nature Geoscience*, vol. 1, no. 12, pp. 864–869, 2008.
- [6] M. Michini, M. A. Hsieh, E. Forgoston, and I. B. Schwartz, “Robotic tracking of coherent structures in flows,” *IEEE Transactions on Robotics*, vol. 30, no. 3, pp. 593–603, 2014.
- [7] M. Ani Hsieh, H. Hajieghrary, D. Kularatne, C. R. Heckman, E. Forgoston, I. B. Schwartz, and P. A. Yecko, “Small and adrift with self-control: using the environment to improve autonomy,” *Robotics Research: Volume 2*, pp. 387–402, 2018.
- [8] A. Hadjighasem, M. Farazmand, D. Blazevski, G. Froyland, and G. Haller, “A critical comparison of Lagrangian methods for coherent structure detection,” *Chaos: An Interdisciplinary Journal of Nonlinear Science*, vol. 27, no. 5, p. 053104, 2017.
- [9] N. Raju and E. Meiburg, “Dynamics of small, spherical particles in vortical and stagnation point flow fields,” *Physics of Fluids*, vol. 9, no. 2, pp. 299–314, 1997.
- [10] I. Benczik, G. Károlyi, I. Scheuring, and T. Tél, “Coexistence of inertial competitors in chaotic flows,” *Chaos: An Interdisciplinary Journal of Nonlinear Science*, vol. 16, no. 4, p. 043110, 2006.
- [11] K. Yao, E. Forgoston, and P. Yecko, “Learning ocean circulation models with reservoir computing,” *Physics of Fluids*, vol. 34, no. 11, p. 116604, 2022.

- [12] E. Forgoston, L. Billings, P. Yecko, and I. B. Schwartz, “Set-based corral control in stochastic dynamical systems: Making almost invariant sets more invariant,” *Chaos: An Interdisciplinary Journal of Nonlinear Science*, vol. 21, no. 1, p. 013116, 2011.
- [13] D. Kularatne, E. Forgoston, and M. A. Hsieh, “Using control to shape stochastic escape and switching dynamics,” *Chaos: An Interdisciplinary Journal of Nonlinear Science*, vol. 29, no. 5, p. 053128, 2019.
- [14] T. Salam, D. Kularatne, E. Forgoston, and M. A. Hsieh, “Adaptive sampling and energy efficient navigation in time-varying flows,” in *Autonomous Underwater Vehicles*, pp. 493–537, Institution of Engineering and Technology, 2020.
- [15] G. You, T. Wong, and S. Leung, “Eulerian methods for visualizing continuous dynamical systems using Lyapunov exponents,” *SIAM Journal on Scientific Computing*, vol. 39, no. 2, pp. A415–A437, 2017.
- [16] Norman Kuring, MODIS Ocean Team, “The Gulf Stream.” <https://earthobservatory.nasa.gov/images/5432/the-gulf-stream>, 2005. [Online; accessed April-2023].
- [17] Lori Perkins, NASA/Goddard Space Flight Center Scientific Visualization Studio, “Aquarius studies Ocean and Wind Flows.” <https://svs.gsfc.nasa.gov/3829>, 2011. [Online; accessed April-2023].
- [18] Jeff Schmaltz, LANCE/EOSDIS Rapid Response, “Bloom off of New Zealand.” <https://earthobservatory.nasa.gov/images/91274/bloom-off-of-new-zealand>, 2017. [Online; accessed April-2023].
- [19] Jesse Allen and Robert Simmon, “Oil Slick Around Mississippi Barrier Islands.” <https://earthobservatory.nasa.gov/images/44466/oil-slick-around-mississippi-barrier-islands/>, 2010. [Online; accessed April-2023].
- [20] M. A. Hsieh, E. Forgoston, T. W. Mather, and I. B. Schwartz, “Robotic manifold tracking of coherent structures in flows,” in *2012 IEEE International Conference on Robotics and Automation*, pp. 4242–4247, IEEE, 2012.
- [21] G. Haller, “Lagrangian coherent structures,” *Annual review of fluid mechanics*, vol. 47, pp. 137–162, 2015.
- [22] K. Mallory, M. A. Hsieh, E. Forgoston, and I. B. Schwartz, “Distributed allocation of mobile sensing swarms in gyre flows,” *Nonlinear Processes in Geophysics*, vol. 20, no. 5, pp. 657–668, 2013.
- [23] M. A. Hsieh, K. Mallory, E. Forgoston, and I. B. Schwartz, “Distributed allocation of mobile sensing agents in geophysical flows,” in *2014 American Control Conference*, pp. 165–171, IEEE, 2014.

- [24] F. Lekien, S. C. Shadden, and J. E. Marsden, “Lagrangian coherent structures in n-dimensional systems,” *Journal of Mathematical Physics*, vol. 48, no. 6, p. 065404, 2007.
- [25] M. R. Allshouse and T. Peacock, “Refining finite-time Lyapunov exponent ridges and the challenges of classifying them,” *Chaos: An Interdisciplinary Journal of Nonlinear Science*, vol. 25, no. 8, p. 087410, 2015.
- [26] A. Aucoin, “Inertial particle transport by Lagrangian coherent structures in geophysical flows,” 2018.
- [27] G. Haller and T. Sapsis, “Where do inertial particles go in fluid flows?,” *Physica D: Nonlinear Phenomena*, vol. 237, no. 5, pp. 573–583, 2008.
- [28] M. Sudharsan, S. L. Brunton, and J. J. Riley, “Lagrangian coherent structures and inertial particle dynamics,” *Physical Review E*, vol. 93, no. 3, p. 033108, 2016.
- [29] M. R. Maxey and J. J. Riley, “Equation of motion for a small rigid sphere in a nonuniform flow,” *The Physics of Fluids*, vol. 26, no. 4, pp. 883–889, 1983.
- [30] J. H. Cartwright, U. Feudel, G. Károlyi, A. de Moura, O. Piro, and T. Tél, “Dynamics of finite-size particles in chaotic fluid flows,” *Nonlinear dynamics and chaos: advances and perspectives*, pp. 51–87, 2010.
- [31] M. Farazmand and G. Haller, “The Maxey–Riley equation: Existence, uniqueness and regularity of solutions,” *Nonlinear Analysis: Real World Applications*, vol. 22, pp. 98–106, 2015.
- [32] P. G. J. Holmes, *Nonlinear Oscillations Dynamical Systems and Bifurcations of Vector Fields*, ch. 2.2 Duffing’s Equation. Springer, 1983.
- [33] D. del Castillo-Negrete and P. Morrison, “Chaotic transport by Rossby waves in shear flow,” *Physics of Fluids A: Fluid Dynamics*, vol. 5, no. 4, pp. 948–965, 1993.
- [34] P. S. Marcus, “Vortex dynamics in a shearing zonal flow,” *Journal of Fluid Mechanics*, vol. 215, pp. 393–430, 1990.
- [35] I. Rypina, M. G. Brown, F. J. Beron-Vera, H. Koçak, M. J. Olascoaga, and I. Udovydchenkov, “On the lagrangian dynamics of atmospheric zonal jets and the permeability of the stratospheric polar vortex,” *Journal of the Atmospheric Sciences*, vol. 64, no. 10, pp. 3595–3610, 2007.
- [36] F. J. Beron-Vera, M. J. Olascoaga, M. G. Brown, H. Koçak, and I. I. Rypina, “Invariant-tori-like lagrangian coherent structures in geophysical flows,” *Chaos: An Interdisciplinary Journal of Nonlinear Science*, vol. 20, no. 1, p. 017514, 2010.

- [37] I. Rypina, M. G. Brown, F. J. Beron-Vera, H. Koçak, M. J. Olascoaga, and I. Udovydchenkov, “On the lagrangian dynamics of atmospheric zonal jets and the permeability of the stratospheric polar vortex,” *Journal of the Atmospheric Sciences*, vol. 64, no. 10, pp. 3595–3610, 2007.
- [38] J. Pedlosky, *Ocean Circulation Theory*. Springer, 1996.
- [39] K. Yao, *Modeling Quasi-Geostrophic Flows with a Reservoir Computing Approach*. PhD thesis, The Cooper Union for the Advancement of Science and Art, 2020.
- [40] Y. LeCun, Y. Bengio, and G. Hinton, “Deep learning,” *Nature*, vol. 521, no. 7553, pp. 436–444, 2015.
- [41] Z. Ghahramani, “Probabilistic machine learning and artificial intelligence,” *Nature*, vol. 521, no. 7553, pp. 452–459, 2015.
- [42] M. Qraitem, D. Kularatne, E. Forgoston, and M. A. Hsieh, “Bridging the gap: Machine learning to resolve improperly modeled dynamics,” *Physica D: Nonlinear Phenomena*, vol. 414, p. 132736, 2020.
- [43] T. Z. Jiahao, M. A. Hsieh, and E. Forgoston, “Knowledge-based learning of nonlinear dynamics and chaos,” *Chaos: An Interdisciplinary Journal of Nonlinear Science*, vol. 31, no. 11, p. 111101, 2021.